Pre-print submitted version

Room temperature vacuum-deposition of $CsPbI_2Br$ perovskite films from multiple-sources and mixed halide precursors.

Ana M. Igual-Muñoz, Javier Navarro-Alapont, Chris Dreessen, Francisco Palazon, Michele Sessolo*, Henk J. Bolink

Instituto de Ciencia Molecular, Universidad de Valencia, C/ J. Beltran 2, 46980 Paterna, Spain.

**E-mail: michele.sessolo@uv.es*

ABSTRACT

Fully inorganic cesium lead halide perovskites, such as $CsPbI_2Br$, show enhanced thermal stability compared to hybrid ones, and are being widely investigated as wide bandgap absorbers for tandem applications. Despite their simple stoichiometry, the preparation of highly crystalline and stable cesium lead halides thin-films is not trivial. In general, high efficiency solar cells based on solution-processed $CsPbI_2Br$ thin films are prepared with high temperature annealing or with the use of chemical additives. In this work we use solvent-free synthesis to investigate the formation of $CsPbI_2Br$ in bulk or in thin-film, via mechanochemical synthesis and multiple-source vacuum deposition, respectively. We demonstrate the importance of fostering halide alloying in the vacuum processing of inorganic lead halide perovskites, which can be attained either by using mixed halide precursors or by increasing the number of precursors (and hence deposition sources). These strategies lead to highly oriented perovskite films even at room temperature, with improved optoelectronics properties. We obtained promising power conversion efficiency of 8.3% for solar cells employing as-deposited perovskites (without any annealing) and of 10.0% for devices based on $CsPbI_2Br$ annealed at low temperature (150 °C). This study allowed us to highlight the most promising processes and strategies to further optimize the material deposition as well as the solar cells architecture.

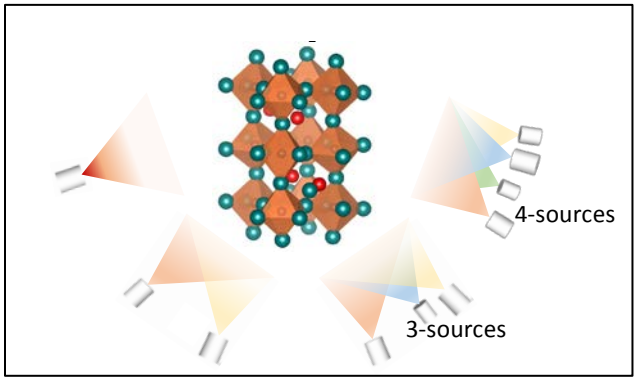

INTRODUCTION

Organic-inorganic (hybrid) perovskites have become one of the most promising semiconductors for application in photovoltaics (PV), since the first perovskite solar cells were reported in 2009.[1] Nowadays, the power conversion efficiencies (PCE) of perovskite solar cells have improved up to 25% for single junction and to 28% for tandem devices with silicon.[2] Those solar cells are based on perovskite absorbers using a combination of, at least, methylammonium (MA) and formamidinium (FA) cations.[3,4] These cations might undermine the thermal stability of the material, which can be partially recovered by their substitution with cesium (Cs^+).[5–7] In general, fully inorganic, cesium lead halide perovskites show enhanced thermal stability compared to hybrid ones.[8–10] They are especially interesting for tandem applications due to their wide bandgap, about 1.7 eV for $CsPbI_3$ and 1.9 eV for the archetypical mixed halide $CsPbI_2Br$.[11,12] In view of these characteristics, inorganic lead halide perovskites are being widely investigated.[13–17] As a result, perovskite solar cells employing inorganic perovskite absorbers have currently achieved PCE exceeding 18% for pure iodide and over 16% for mixed halide compounds. [18–21]

Despite their simple stoichiometry, the preparation of highly crystalline and stable cesium lead halides thin-films is not trivial. The stable phase at room temperature for $CsPbI_3$ is an insulating, orthorhombic phase ("yellow" phase), and the perovskite ("black") phase can only be obtained upon annealing at high temperatures (> 300 °C).[22–24] The inclusion of bromide, as in $CsPbI_2Br$, favors the stabilization of the perovskite phase at lower temperature, although it implies a widening of the bandgap as a consequence of the substitution of iodide with a more electronegative halide.[11,25–28] In general, high efficiency (>15%) solar cells based on solution-processed $CsPbI_2Br$ thin films are prepared with thermal treatments at temperatures ranging from 150 °C to 300 °C. Additionally, in most cases other synergistic approaches are used to foster the perovskite crystallization from solution, such as the addition of group 1 and group 2 ions,[29–33] divalent transition metals,[34–39] rare earths,[40–42] organic cations/anions,[43–48] or the use of interface materials promoting

the perovskite formation and passivation, notably metal oxides (in particular ZnO and its derivatives)[49–54] and novel organic hole transport layers.[55–58]

An alternative solvent-free technique to deposit perovskite thin-films is thermal vacuum deposition.[59,60] Vacuum deposition methods are intrinsically additive (suited for tandem devices),[61–63] and can be used to deposit highly crystalline perovskite films at room temperature.[64] Importantly, vacuum deposition allows the preparation of perovskite films with controllable thickness (not limited by the solubility of the precursors)[65–67] and composition,[68–71] although the latter might be limited by the number of available deposition sources, as well as by the available stable single phase compounds in the compositional phase space. The formation of perovskite films by thermal vacuum deposition differs substantially from solution-processing, due to the absence of solvents, intermediate species, and distinctive crystallization kinetics as a function of the stoichiometry and temperature.[72–74] Vacuum-deposited, cesium lead halide perovskite films and solar cells have been also investigated. In particular, $CsPbI_3$ as well as $CsPbI_2Br$ films have been prepared by dual-source vacuum deposition, and applied to solar cells.[75–79] Stabilization of the perovskite $CsPbI_3$ phase has been achieved by working with Cs-rich compositions, and by simultaneous heating of the substrate holder during deposition.[80] Alternatively, the sequential deposition of multiple very thin films of CsX and PbX_2 (X = I, Br) have also proven to be a reliable method to obtain stable and crystalline films,[81] with record $CsPbI_2Br$ solar cells exhibiting efficiency of 13%.[82] In all these cases, however, the as-deposited films were annealed at temperatures ranging from 260 °C to 320 °C, which might limit their compatibility with temperature-sensitive substrates, such as textiles or plastic foils,[83] and with narrow bandgap perovskite absorbers when targeting tandem solar cells.

In this work, we study the properties of $CsPbI_2Br$ films prepared by thermal vacuum deposition. We focus on films deposited at room temperature (RT) and with mild annealing at 150 °C, which would be compatible with the aforementioned applications. We compare the properties of perovskite films deposited by single-, dual-, triple-, and quadruple sources, using CsI, CsBr, PbI_2 and $PbBr_2$ as precursors (Scheme 1). We also use another solvent-free method to prepare perovskite powders, mechanochemical synthesis,[84] to demonstrate the challenges in achieving alloyed halide compounds. Finally, we prepared fully-vacuum deposited solar cells, obtaining promising PCE of 8% for $CsPbI_2Br$ films prepared at room temperature, and 10% for those annealed at 150 °C.

RESULTS AND DISCUSSION

In order to evaluate the stability and the ease of formation of $CsPbI_2Br$, we initially tested mechanochemical synthesis, ball-milling the CsBr and PbI_2 precursors. We have previously shown the mechanochemical

synthesis of cesium lead trihalide perovskites $CsPbX_3$ (X = I, Br, Cl) powders, as well as their single-source vacuum deposition into highly crystalline thin films.[85] In those experiments we showed that $CsPbI_3$ was not obtained in its perovskite phase by ball-milling of the precursors. This observation suggests that the mixed halide $CsPbI_2Br$ might also be challenging to obtain by mechanochemical synthesis at RT. Indeed, when ball-milling at RT an equimolar amount of CsBr and PbI_2, we obtained a mixture of different phases, as evidence by the X-ray diffraction (XRD, Figure S1). The diffractogram of the ball-milled sample can be fitted considering the coexistence of two phases, a perovskite and a non-perovskite one. The presence of the two phases is apparent considering the low-angle diffractions (2θ = 10°-15°), where the first peak around 2θ = 10° cannot be ascribed to the perovskite phase, which is characterized by the reflections around 2θ =14°. While both phases correspond to the same space group (62; orthorhombic crystal system), one maintains the overall 3D perovskite structure with a slight distortion of the PbX_6 octahedra, while the "non-perovskite" phase consists of partially disconnected PbX_6 octahedra (Figure S2).[86] Since the distorted perovskite phase is the most commonly reported one for $CsPbBr_3$ at RT and the non-perovskite (sometimes called "yellow phase") is the most commonly found for $CsPbI_3$, it could be thought that our ball-milled sample consists of a mixture of pure-bromide and pure-iodide phases (*i.e.*, $CsPbBr_3$ + $CsPbI_3$). Nevertheless, the lattice parameters obtained for both phases formed by mechanochemical synthesis are clearly different than those expected for pure-halide compounds (see Table S1). In particular, the perovskite phase shows lattice constants larger than the reference $CsPbBr_3$, pointing to the incorporation of the larger I^- anion. Similarly, the non-perovskite phase shows lattice parameters slightly smaller than the reference $CsPbI_3$, suggesting the incorporation of the smaller Br^- anion. These observations imply that alloying of halides occurs in both the non-perovskite and perovskite phases. Previous reports on the mechanochemical synthesis of mixed iodide/bromide $CsPb(I_{1-x}Br_x)_3$ perovskites also mentioned that these compounds cannot be obtained at RT, but only after annealing at elevated temperatures (> 250 °C).[87] In our case, we were not able to obtain phase-pure $CsPbI_2Br$ even after melting of the two precursors at 650 °C in nitrogen atmosphere (Figure S1). A possible origin of the different reaction routes, is that all our experiments are carried out in an inert atmosphere (nitrogen-filled glove-box), while the previously reported mechanochemical synthesis was done in air. The XRD of the melted sample closely resemble that of the ball-milled compound, with the addition of a new phase corresponding to Cs_4PbX_6, (labelled "4-1-6" for simplicity). The occurrence of this phase is mostly visible by the new (although relatively weak) peaks at 2θ = 12.0°-12.5°. Several previous reports have observed the appearance of this phase and its possible conversion into or from $CsPbX_3$ under different conditions.[88–90] In both samples obtained by mechanochemical synthesis and by melting, the presence of the perovskite phase can be identified also by its optical absorption (Figure S3), which corresponds to the band-to-band transition of $CsPbI_2Br$ at approximately 1.85-1.90 eV.

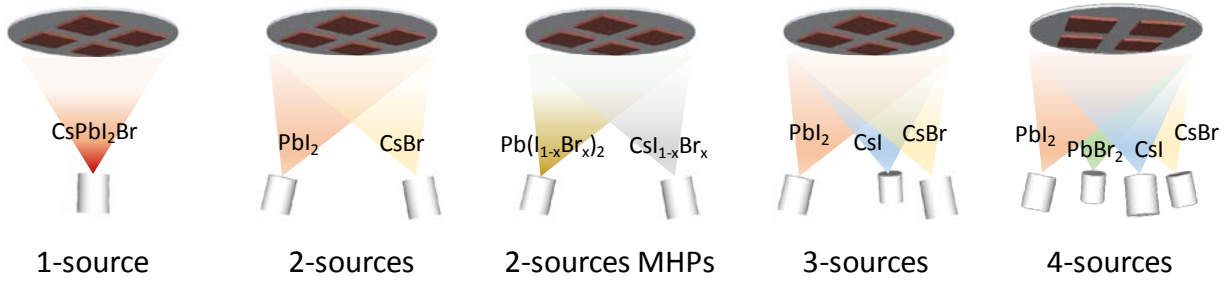

Scheme 1. Schematics of the types of thermal vacuum deposition methods investigated in the preparation of $CsPbI_2Br$ thin-films. For the deposition from 1-source or 2-sources MHPs (mixed halide precursors, x = 1/3), the compounds to be sublimed were prepared by melting. 3-sources vacuum deposition was performed at 0.5 Å/s (3-sources slow) and 2.0 Å/s (3-sources fast).

In order to prepare thin films, we initially tested the single-source (referred to as "1-source") vacuum deposition of the as-prepared ball-milled and melted compounds obtained by solid state reaction of CsBr and PbI_2 in stoichiometric proportion. The materials were loaded into a ceramic crucible and rapidly heated in vacuum (5 °C/s, base pressure 10^{-6} mbar) up to the maximum temperature compatible with our setup, 750 °C. The fast heating ramp and the high target temperature were chosen to minimize the decomposition of the material into its precursors, which have different volatility (melting points at RT for PbI_2 and CsBr are 410 °C and 636 °C, respectively).[91] The resulting films were initially analyzed by XRD (Figure 1a), showing the coexistence of several phases with a predominance of PbI_2, whose main peak appears at 2θ = 12.8°. Other phases present in the films include the desired $CsPbX_3$ perovskite phase as well as the Cs-rich Cs_4PbX_6 (labelled "4-1-6") and the Pb-rich $CsPb_2X_5$ (labelled "1-2-5"). Overall, it is evident that single-source deposition leads to a very inhomogeneous composition for this type of compound. The as-deposited films were also analyzed by scanning electron microscopy (SEM, Figure 2a), showing a rather homogeneous morphology, with very fine grains and no relevant features. The bandgap energy (E_g) estimated from the Tauc plot of the corresponding optical absorbance (Figure 3) is 1.94 eV, slightly higher compared to the powders as a consequence of the PbI_2 segregation (the perovskite phase is hence bromide-rich). Subsequently, we performed the dual-source vacuum deposition (referred to as "2-sources") of $CsPbI_2Br$, consisting in the simultaneous sublimation of CsBr and PbI_2 upon calibration of their respective deposition rates. The XRD pattern of an as-deposited film (Figure 1b) is mainly composed by a pure perovskite phase, without any preferential orientation, which is characteristic of powders with similar compositions.[87,92] The lack of orientation, otherwise observed for cesium lead halides and other vacuum-

deposited perovskite films,[93,94] might be related with the porosity observed by SEM (Figure 2b), suggesting a limited connectivity and hence uncorrelated growth of the grains. It is interesting to point out that phase-pure $CsPbI_2Br$ can be readily obtained through vacuum deposition, while it cannot be formed by mechanochemical synthesis even after thermal treatment at 650 °C. The likely main difference is that in vacuum deposition, where atomization/fragmentation of the precursors takes place, the atoms/clusters condense on a cold substrate, essentially freezing the structure and resulting in well-mixed compounds. When heating at high temperature, the cooling process is slow, resulting in phase segregation as dictated by thermodynamics. The reaction kinetics are very different as well, as by vacuum sublimation the atomic fragments deposit with high kinetic energy, whereas the heating after mechanochemical synthesis is done without friction.

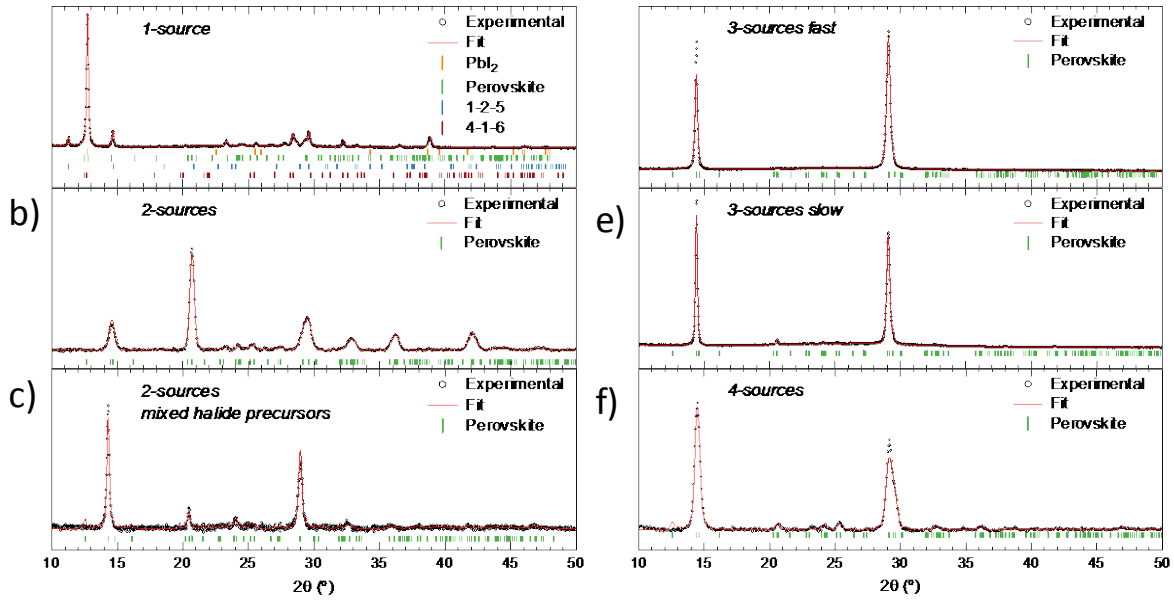

Figure 1. XRD pattern obtained from $CsPbI_2Br$ thin-films deposited with several different vacuum-deposition techniques (as indicated in each graph). Open circles are raw data, red lines are whole-pattern Le Bail fits, and vertical lines represent calculated Bragg's reflections for different phases. Slight differences in the measurement conditions prevent relating peak width to microstructural properties (e.g., grain size) of the samples.

Although the unit cell volume for the 2-sources $CsPbI_2Br$ (907 $Å^3$) confirms halide mixing in the as-deposited films (it is larger than that of pure $CsPbBr_3$, 797 $Å^3$), we decided to investigate the dual-source deposition starting from mixed halide precursors (MHPs). Pre-alloying of halides in the precursors might

help the formation of a perovskite with a more homogeneous structure. For this, we carried out the solid state reactions by mixing $PbBr_2$ with PbI_2 and CsBr with CsI, in 1:2 molar ratios in both cases. The ratio was chosen in view of the desired $CsPbI_2Br$ perovskite stoichiometry, where the Br:I ratio is also 1:2. The XRD patterns of the as-prepared compounds, both ball-milled or melted, are shown in Figure S5 and S6. We observed that after reaction, the reflections belonging to CsI and CsBr are shifted to higher and lower angles, respectively, indicating the incorporation of bromide into CsI and vice versa (Figure S5). On the other hand, an alloyed $Pb(I_{1-x}Br_x)_2$ phase is indeed obtained when reacting PbI_2 and $PbBr_2$, although not quantitatively as suggested by the presence of XRD peaks of the precursors (Figure S6). These observations confirm that halide alloying is not favored even for these simple binary precursors. Based on the XRD characterization, we choose melting as the technique to prepare the MHPs to be used in dual-source vacuum deposition ("2-source MHP"). The experiment consisted in melting $PbBr_2$ with PbI_2 and CsBr with CsI, in 1:2 molar ratios, in separated heated crucible in a vacuum chamber (not evacuated, in nitrogen atmosphere). After melting and cooling to RT, the chamber was evacuated to 10^{-6} mbar and the MHPs were co-deposited using the calibration factors previously calculated for the 2-source deposition, while maintaining the substrates at RT. Remarkably, the films obtained from MHPs consist in phase-pure $CsPbI_2Br$, with preferred orientation along the (110) and (002) directions (Figure 1c), i.e. perpendicular to the substrate surface. The as-deposited films also show a more compact morphology (compared to those prepared by 2-source deposition of the single halide precursors), with small but well defined grains homogeneously organized on the sample surface (Figure 2c). The low unit cell volume (891 $Å^3$) and phase purity suggest a homogeneous halide mixing, resulting in a bandgap energy of 1.90 eV (Figure 3). Hence it seems that fostering halide alloying can indeed enhance the quality of mixed halide perovskite deposited by vacuum methods.

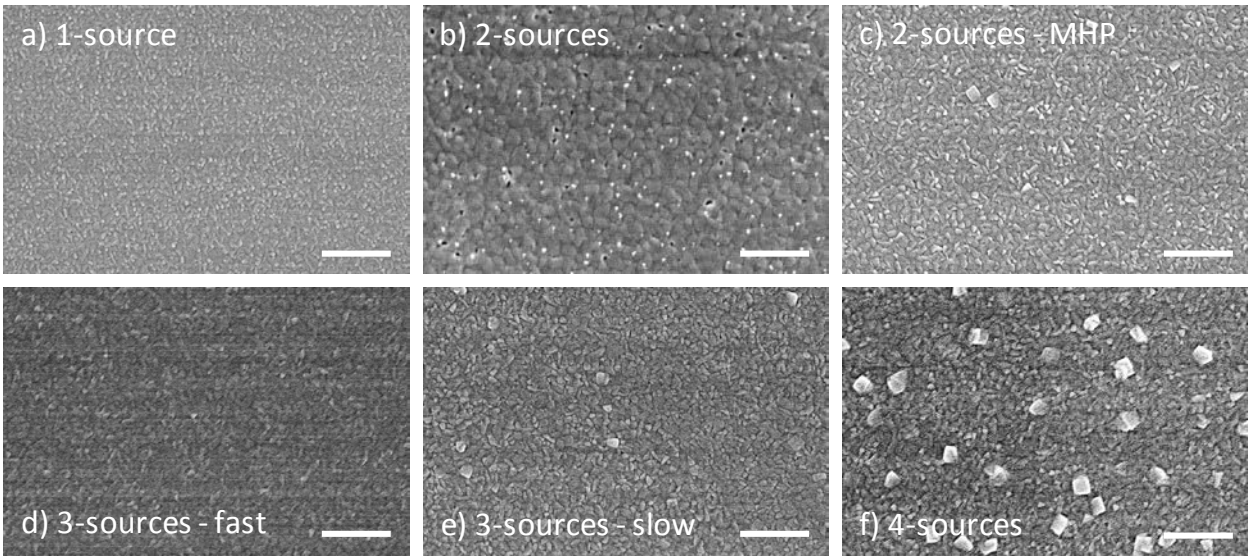

Figure 2. Scanning electron microscopy images of the surface of $CsPbI_2Br$ thin-films deposited with several different vacuum-deposition techniques (as indicated in each graph). Scale bar is 500 nm in all images.

One of the possible drawbacks of depositing mixed halide precursors is the formation of films with a compositional gradient, as the high vapor pressure constituent vaporizes more rapidly than the low vapor pressure material.[95] This might happen as CsI and PbI_2 have larger vapor pressure as compared to their bromide analogues.[96] An alternative way to enhance halide alloying and homogeneity in perovskite vacuum-deposition is the use of more than two deposition sources.[97] Hence, we investigated a 3-source deposition process, consisting in the simultaneous sublimation of CsI, CsBr and PbI_2 from separate thermal sources. In vacuum deposition of compounds, such as metal halides, the material might vaporize with a range of species, from atoms to clusters of molecules to dissociated or partially dissociated molecules. These small fragments then condense and react with each other on the substrate surface forming a solid film. In the process, the deposition rate plays a crucial role, as an excessively fast evaporation would result in an increased content of amorphous material. We therefore tested the 3-source vacuum deposition of $CsPbI_2Br$ at different deposition rates (measured at the substrate): 2.0 Å/s ("3-sources fast") and 0.5 Å/s ("3-sources slow"), with the substrates kept at RT. The diffractograms of both compounds (Figure 1 d-e) show a phase-pure perovskite with high crystallinity and no signs of precursors or derivatives. Both samples have a strong preferential orientation along the (110) and (002) directions, with the perovskite film deposited with slow rate showing narrower diffraction peaks, which might suggest the presence of larger crystallites. Although not apparent, this fact might be correlated with the improved morphology of $CsPbI_2Br$

deposited at 0.5 Å/s (Figure 2e), when compared with the film deposited at 2.0 Å/s (Figure 2c). These films exhibit a very similar bandgap energy of 1.88 eV (slow) and 1.89 eV (fast), with the "3-source slow" layers showing a more intense optical absorption (for the same thickness of 250 nm) over the whole spectral region (Figure 3).

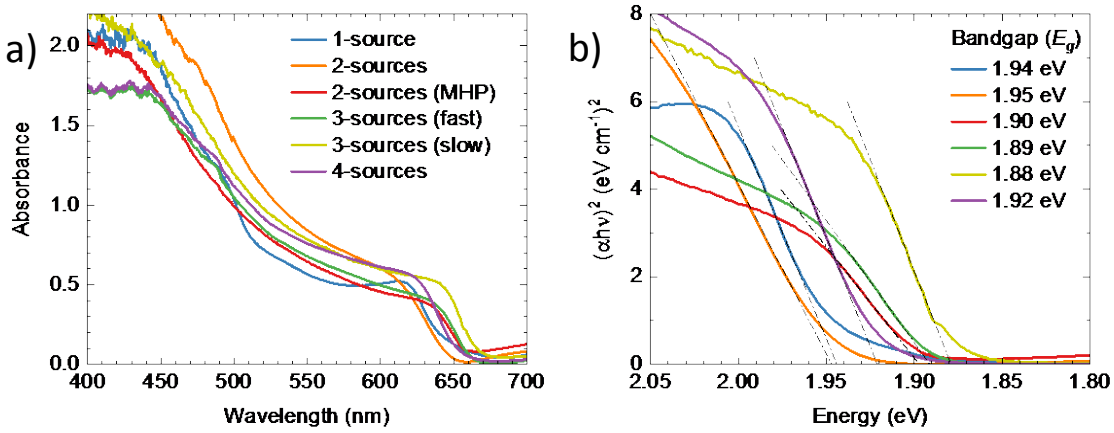

Figure 3. a) Absorbance and corresponding b) Tauc plots (with the estimated bandgap energy) spectra for $CsPbI_2Br$ thin-films deposited on glass with several different vacuum-deposition techniques. Thickness for all films is 250 nm.

A complementary 3-source deposition scheme, which can also lead to the formation of $CsPbI_2Br$ films, consists in the simultaneous sublimation of CsI, PbI_2 and $PbBr_2$. The as-prepared films obtained through this process showed the expected absorption profile and bandgap (1.93 eV, Figure S7a-b), confirming the formation of the perovskite phase at RT, using mixed lead halide precursors. However, in this case the resulting films were found to be particularly unstable in ambient atmosphere, to a point that we were note able to collect a single XRD scan before complete discoloration and degradation of the sample (Figure S7c). Considering that phase pure and stable films were obtained using CsI, CsBr and PbI_2 as precursors (discussion above), it appears more important to foster halide mixing of the cesium halides precursor, likely in view of the larger lattice energies of the ionic compounds CsI and CsBr, compared to PbI_2 and $PbBr_2$. As a final test, we performed the deposition of $CsPbI_2Br$ employing 4 sources (co-sublimation of CsI, CsBr, PbI_2, and $PbBr_2$) to investigate whether the use of both iodide and bromide precursors for Cs and Pb during the sublimation process provides advantages in the formation of the perovskite film. The XRD pattern (Figure 1f) of as-deposited "4-sources" films can again be fitted with a single and pure perovskite phase. However, the presence of several diffraction signals in the range $20° \leq 2\theta \leq 26°$ (and of others at $2\theta > 30°$)

indicates that this material has lower preferential orientation compared to the 2- and 3-sources deposited one. The surface morphology of films deposited by 4-sources vacuum deposition show homogenous coverage with very fine grains (diameter < 50 nm), and the formation of cuboids with edges of approximately 100 nm (the low dimensions of these structure prohibit their structural/compositional analysis). Similar structures, although much scarcer and smaller, have been observed for the "2-sources MHP" and the "3-sources slow" (Figure 2c and 2e, respectively), which might suggest that their crystallization is favored either by enhanced halide alloying or slower growth. The absorption onset of the "4-sources" $CsPbI_2Br$ is essentially unaltered, showing the excepted E_g = 1.92 eV.

To shortly summarize, we demonstrated the successful room temperature deposition of $CsPbI_2Br$ films with high crystallinity, preferential orientation, homogeneous morphology and the expected bandgap of approximately 1.9 eV. This was possible when subliming MHPs or by increasing the number of deposition sources (hence of precursors). In view of the favorable properties of the $CsPbI_2Br$ films presented above, we used them as the light-absorbing layer in fully vacuum-deposited perovskite solar cells. We fabricated p-i-n solar cells with the structure reported in Figure 4a. Briefly, indium tin oxide (ITO) transparent electrodes were coated with MoO_3 (5 nm) to enhance hole transfer between ITO and the hole transport layer (HTL), a 10 nm thick film of *N*4,*N*4,*N*4″,*N*4″-tetra([1,1′-biphenyl]-4-yl)-[1,1′:4′,1″-terphenyl]-4,4″-diamine (TaTm, 10 nm). Afterwards, a 250 nm thick $CsPbI_2Br$ film was deposited on top with the different sublimation methods described before. We did not evaluate in devices the perovskite films deposited by single-source vacuum-deposition ("1-source"), in view of their unfavorable morphological and structural properties. The perovskite films were capped with an electron transport layer (ETL, C_{60}, 25 nm), and a thin (8 nm) film of bathocuproine (BCP) was used to ensure ohmic contact in between the ETL and a silver electrode (100 nm thick). The use of such thin selective transport layers in a planar diode configuration is justified by the very homogeneous morphology and very low roughness of the $CsPbI_2Br$ films (Figure S8), which is in general a benchmark of vacuum deposited perovskite films when compared to their solution-processed analogous.

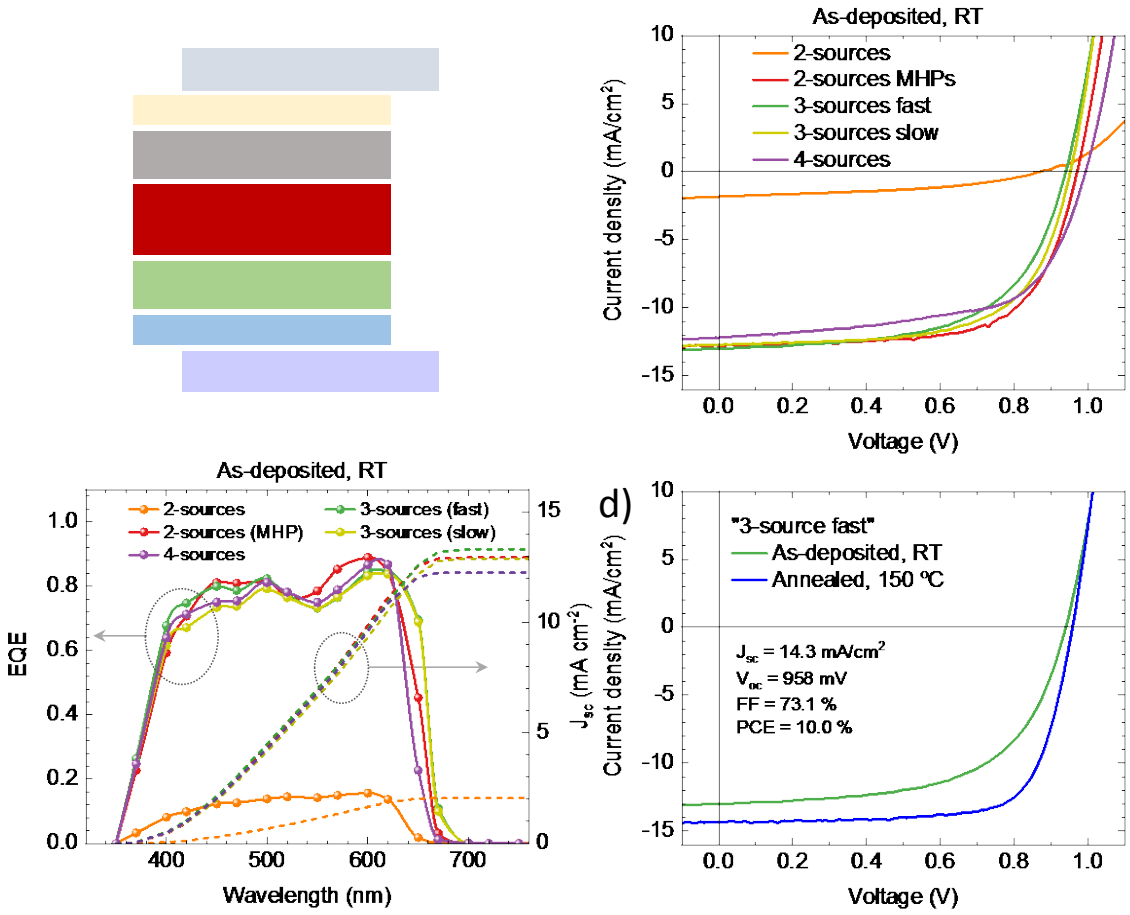

Figure 4. a) Solar cell layout, b) J-V curves under illumination and c) EQE spectra for a series of solar cells employing $CsPbI_2Br$ deposited at room temperature with the different vacuum techniques. The corresponding short circuit current density, obtained by integration of each EQE spectra over the reference AM1.5 solar irradiance spectrum, is reported on the right axis. d) J-V curves of solar cells with $CsPbI_2Br$ prepared by 3-sources vacuum deposition at the rate of 2.0 Å/s (fast), either at room temperature (green) or with annealing at 150 °C for 5 minutes (blue).

The current density vs. voltage characteristics (J-V) under simulated solar illumination for the entire series of solar cells are reported in Figure 4b. J-V curves are reported in reverse voltage scan (from open to short circuit (curves in both scan directions are reported in Figure S10). We noted some extent of hysteresis in the devices, which denotes the presence of both charge accumulation and ionic motion in the device. The characteristic photovoltaic parameters extracted from the J-V curves are presented in Figure 5. One can immediately notice how the device with the perovskite deposited from 2-sources underperforms as compared to the others. This type of vacuum deposition (co-sublimation of CsBr and PbI_2) is the only one

reported in the literature, and is known to lead to efficient devices only after annealing at high temperature >260 °C.[79] The corresponding external quantum efficiency (EQE) spectrum shows a very limited photocurrent generation over the whole spectral range. These observations correlate with the poor structural (Figure 1b) and morphological (Figure 2b) features of the material. Improving halide alloying (by using MHPs) leads to a strong improvement of the solar cells performance, with good rectification (fill factor, FF > 65%) and open circuit voltage (V_{oc} = 970 mV). The short circuit current density (J_{sc}) was found to be as high as 12.8 mA/cm^2, a consequence of the rather constant and high spectral response over the whole visible spectrum (Figure 4c). The resulting PCE was found to be 8.3%, which is remarkable for solar cells based on inorganic lead halide perovskites deposited at RT. From the solar cells prepared with the "3-sources" perovskites, we observed similar performance parameters. The J_{sc} was found to be approximately 13 mA/cm^2, slightly higher compared to the "2-sources MHP" based devices due to the enhanced response in the red, a consequence of the narrower bandgap (Figure 3b). Interestingly, the FF was found to be higher (65% vs. 60%) for the solar cells with $CsPbI_2Br$ prepared with the slowest deposition rate (0.5 Å/s, "3-sources slow"), suggesting that a slow crystallization might favor charge transport within the film, due to the formation of larger crystallites and more oriented materials. However, the observed photovoltage was rather similar for the two devices (940 and 950 mV for the fast and slow depositions, respectively), resulting in a similar PCE of 7.7% and 7.3% for cells using $CsPbI_2Br$ deposited at 0.5 Å/s and 2.0 Å/s, respectively. We note that lead halide perovskite thin films have been reported with different orientations, yet without a clear understanding of the factors governing it nor of the implications for their optoelectronic properties.[74] Similar efficiency was observed for solar cells using the "4-sources" deposited perovskite, with a lower photocurrent (11 mA/cm^2) but with the largest V_{oc} of 1 V, indicating a reduction of the non-radiative recombination rate. Overall, we can conclude that improved alloying of the different metal halides, either by the synthesis of mixed precursors or through the use of additional deposition sources, can indeed help the formation of high quality cesium lead halide perovskites at room temperature. Importantly, we observed that halide alloying results in preferentially oriented films, which leads to the best performance when used in solar cells. Indeed, the only sample (aside from 1-source which we excluded from this discussion) which is not oriented, the simple 2-sources $CsPbI_2Br$, is the one that gives by far the worst photovoltaic performance.

We also explored the effect of a short annealing at low temperature (150 °C for 5 minutes) on the optoelectronic properties of the $CsPbI_2Br$ films. We choose this temperature as it would be compatible with most flexible plastic substrates as well as with tandem architectures.[83] The J-V curves under illumination and corresponding spectral response for the entire series of solar cells with annealed $CsPbI_2Br$ layers are reported in Figure S11 (scans in both directions are reported in Figure S12). The characteristic photovoltaic parameters extracted from the J-V curves are presented in Figure 5 together with the RT data.

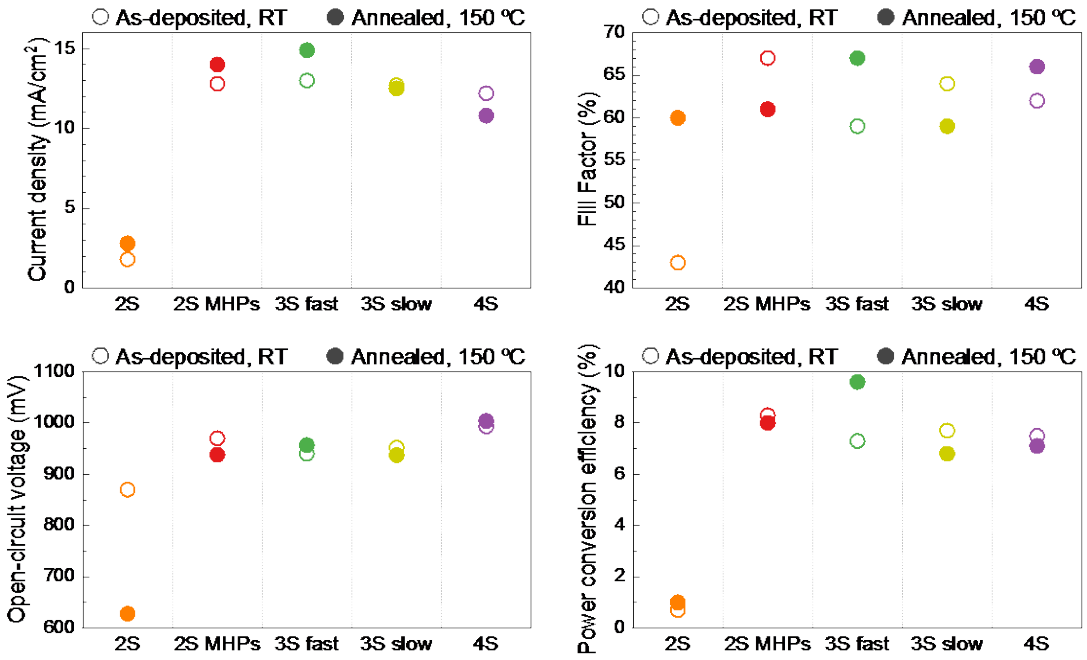

Figure 5. Photovoltaic parameters extracted from J-V scans in reverse bias (from open to short circuit) for solar cells with $CsPbI_2Br$ films either as-deposited (empty symbols) or annealed at 150 °C for 5 minutes (full symbols).

With this moderate annealing, the J_{sc} was found to be unvaried or to increase slightly, in the latter case due to an enhanced response of the devices in the blue region of the spectrum (Figure S11b). On the other hand, the FF decreased of about 5% absolute for the perovskites prepared by 2-sources with MHPs and by 3-sources at slow rate, while it improved for the other samples. Interestingly, the photovoltage was unvaried upon annealing for all samples except for the simple 2-sources deposited one, confirming that a good perovskite semiconductor is formed already at room temperature. The overall efficiency was found similar for the devices based on $CsPbI_2Br$ with and without annealing, with the exception of those obtained by fast deposition (2 Å/s) from 3-sources. The solar cells based on this material and annealed at 150 °C showed the highest efficiency among the series, with the best pixel having a PCE of 10.0%. Despite the hysteresis observed between J-V scans in forward and reverse bias, the power output measured at the maximum power point was found to be rather stable, with an efficiency of 9.8% over an hour of measurement (Figure S12f). In view of the superior thermal stability of inorganic perovskite (compared to the hybrid counterparts), we evaluated the stability of unencapsulated solar cells in inert atmosphere and continuous thermal stress at 85 °C. The best solar cell configuration (3-source fast, annealed at 150 °C) was found to retain 90% of the initial power efficiency after 10 days at 85 °C in the dark (Figure S13).

In spite of the promising performance of the low-temperature deposited $CsPbI_2Br$ solar cells, their efficiency is far from the maximum theoretical one (approximately 25% for a bandgap of 1.9 eV).[98] To shed light on the limitations of the devices, we investigated the EQE in the bandgap region and the photoluminescence (PL) response (Figure 6) of the best working device based on annealed "3-sources fast" perovskites (The corresponding J-V characteristics are shown in Figure 4d). From the sensitive EQE measurement one can extract the bandgap E_g, the radiative limit of the open-circuit voltage $V_{oc,rad}$ and the Urbach energy E_U, assuming that the EQE scales linearly with the absorption (see Table 1).[99,100] The Shockley-Queisser limit of the short-circuit current density ($J_{sc,max}$), the maximum fill factor (FF_{max}) and power conversion efficiency (PCE_{max}) can also be estimated for a specific E_g.[101,102]

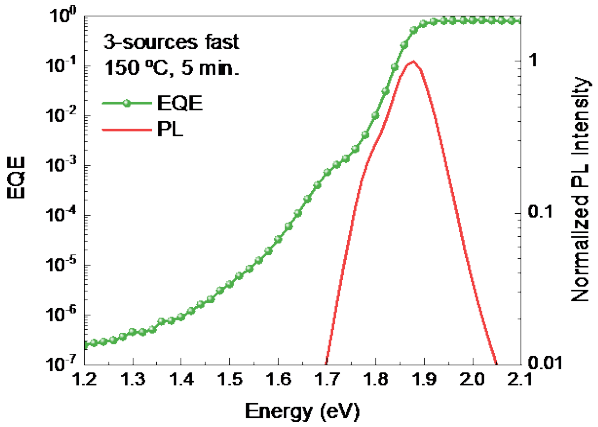

Figure 6. Sensitive EQE spectrum and PL measurements of the solar cell based on the $CsPbI_2Br$ film prepared by 3-sources fast vacuum deposition with annealing.

From the comparison of these maximum (theoretical) values with the measured ones it is clear that the main limitations of the device are the V_{oc} and, to a lesser extent, the FF. The FF scales with the V_{oc} so that with the measured V_{oc} and the ideality factor of 1 (Figure S14a), the ratio FF/FF_{max} lies at 84.1%.[103] However, this is only true for the best solar cell prepared in this series, where otherwise the FF was low on average (Figure 5). This indicates that there are significant resistive losses in the device, which might originate from shunts, from energy barriers resulting from the misalignment between the transport layers and perovskite energy levels, or from a low conductivity of the perovskite itself. The J_{sc} could also suffer from these effects, but in our case is rather high and mainly limited by reflection losses and a non-unitary absorption due to the not-optimized layer thickness. The trend of intensity-dependent current density for the same device might suggest hindered charge extraction (increased recombination) at high light intensity, as the power

factor α becomes < 1 (Figure S14b). The high losses in V_{oc} are common to wide-bandgap perovskites and are usually attributed to photo-induced phase segregation or energy level misalignment.[104] In both the EQE and the PL spectra in Fig 6, an extra component can be observed at low energies (at 1.7 eV and 1.78 eV, respectively), which might account for a voltage loss.

Table 1. Solar cell parameters for the device with "3-sources fast" $CsPbI_2Br$ annealed at 150 °C in the radiative limit and comparison to the measured values. E_g, $V_{oc,rad}$ and E_U are extracted from the EQE measurement in Fig 6. The FF in brackets shows the FF limit without resistive losses obtained by taking into account the measured V_{oc}.

E_g/q (V)	1.870	E_U (meV)	17.96
$V_{oc,rad}$ (V)	1.563	$V_{oc}/V_{oc,rad}$ (%)	61.3
$J_{sc,max}$ (mA/cm^2)	17.7	$J_{sc}/J_{sc,max}$ (%)	80.8
FF_{max} (%)	91.7 (86.9)	FF/FF_{max} (%)	79.7 (84.1)
PCE_{max} (%)	25.4	PCE/PCE_{max} (%)	39.4

The PL feature might be a sign of weak phase segregation; however, this is limited to few regions where the low energy component can be appreciated, as shown in the PL maps in Figure S15. On the other hand, the EQE secondary absorption lies at an energy even lower than that of pure $CsPbI_3$ (1.72 eV) and was obtained at low illumination intensities (≈ 0.001 sun) where phase segregation is usually not occurring. Therefore, the EQE feature is likely an effect originating from misalignment of energy levels between the perovskite and the transport layers, or from the C_{60} itself, which can lead to a photocurrent at very similar energies.[105] This hypothesis is supported by the fact that n-i-p devices using SnO_2 as the ETL (without C_{60}) do not show this feature in the EQE spectrum (Figure S16). Therefore, it might be necessary to find alternative electron transport layers for these and other wide bandgap perovskite solar cells. Finally, the Urbach energy, extracted by fitting the EQE tail between 1.78 eV and 1.85 eV, is of only 18 meV, lower than the thermal energy at room temperature which is crucial for high-performing devices.[106]

CONCLUSION

We demonstrate the room temperature formation of $CsPbI_2Br$ using dry vacuum sublimation processes. The perovskite formation is achieved through a number of different methods with increasing level of complexity. We performed the single-source deposition of previously prepared perovskite powders, which

lead to a mixture of phases and unreacted compounds. We then compared the 2-sources sublimation using either CsBr and PbI_2 or pre-synthesized mixed halide precursors. The superior quality of the latter process highlights the importance of fostering halide alloying in the vacuum processing of inorganic lead halide perovskites. A similar effect can be attained by increasing the number of precursors (and hence deposition sources) to a 3- or 4-sources processes. We observed that these methods led to strongly oriented perovskite films at room temperature, and this orientation was found to be beneficial for the photovoltaics behavior of the semiconductors. We also explored the effect of the sublimation rate, and found that slow sublimation of the precursors leads to $CsPbI_2Br$ films with better structural and optical properties. Importantly, all these processes were performed while maintaining the substrate at room temperature. Overall, we obtained promising power conversion efficiency of 8.3% for solar cells employing as-deposited perovskites (without any annealing) and of 10.0% for devices based on $CsPbI_2Br$ annealed at low temperature (150 °C). Through optoelectronic analysis, we found the open-circuit voltage to be the main limitation of these devices, most likely due to the use of non-optimal electron transport layers.

EXPERIMENTAL SECTION

Materials. Cesium bromide (CsBr, >99%), lead(II) bromide ($PbBr_2$ [perovskite precursor]) and cesium iodide (CsI, >99%) were purchased from Tokyo Chemical Industries (TCI), Molybdenum oxide (MoO_3), bathocuproine (BCP) and lead(II) iodide (PbI_2, 99.999%) from Lumtec, *N4,N4,N4",N4"*-tetra([1,1'-biphenyl]-4- yl)-[1,1':4',1"-terphenyl]-4,4"-diamine (TaTm) from Novaled GmbH and C60 was obtained from Sigma-Aldrich.

Solid state synthesis of perovskite and mixed halide precursors. (1) *$CsPbI_2Br$ by ball-milling*: Stoichiometric amounts of CsBr and PbI_2 powders (1:1) were mixed inside a nitrogen-filled glovebox. Then, approximately 4 g of the mixed precursor powders were introduced inside 10 mL zirconia ball mill jars with two zirconia beads of 10 mm in diameter. The jars were closed under nitrogen so that the powders were not exposed to air. Then, ball milling was performed with an MM-400 shaking ball mill from Retsch, at a frequency of 30 Hz for 99 min. (2) *Mixed halide precursors by ball-milling*: CsBr/CsI and $PbBr_2/PbI_2$ powders (1:2) were weighed in a microbalance. Then, approximately 4 g of the mixed precursor powders were introduced in 10 mL zirconia ball mill jars with two zirconia beads (diameter 10 mm). The jars were closed under nitrogen so that the powders were not exposed to air. Then, ball milling was performed with an MM-400 shaking ball mill from Retsch, at a frequency of 30 Hz for 99 min. (3) *$CsPbI_2Br$ by melting*: CsBr and PbI_2 where weighed in a microbalance with stoichiometric quantities. The powders were introduced in a thermally controlled crucible and heated in nitrogen atmosphere until complete melting (650

°C for 2 minutes). (4) *Mixed halide precursors by melting***:** stoichiometric amounts of CsBr and CsI where weighed in a microbalance to obtain $CsI_{1-x}Br_x$ (x = 1/3). Afterwards, the powders were introduced in a thermally controlled crucible and heated in nitrogen atmosphere until complete melting (650 °C for 2 minutes). Stoichiometric quantities of $PbBr_2$ and PbI_2 where weighed in a microbalance to obtain $Pb(I_{1-x}Br_x)_2$ (x = 1/3). Afterwards, the powders were introduced in a thermally controlled crucible and heated in nitrogen atmosphere until complete melting (420 °C for 2 minutes).

$CsPbI_2Br$ thin-films deposition. All vacuum deposition runs were carried out in a custom-made chamber (Vaksis) integrated in a nitrogen-filled glovebox. The chamber is equipped with four evaporation sources (CreaPhys) fitted with ceramic crucibles and independent temperature controllers and shutters. A dedicated QCM sensor is installed above each source plus one close to the substrate for the overall deposition rate measurement. The base pressure at the beginning of the deposition was 10^{-6} mbar. All the sources were individually calibrated for its respective material. If not otherwise specified, the thickness of the films used in this study was 250 nm. 1-source vacuum deposition: after melting of the precursors in a crucible as detailed above, the chamber was evacuated and the material was sublimed at 750 °C for 1 minute, obtaining a films with thickness of approximately 700 nm. Multi-source vacuum deposition: all materials were co-deposited after calibration of their deposition rates, using 2, 3 or 4 sources simultaneously, with a total deposition rate of 2 Å/s (if not otherwise stated).

Device Preparation. ITO-coated glass substrates were subsequently cleaned with soap, water and isopropanol in an ultrasonic bath, followed by UV-ozone treatment. They were transferred to a nitrogen-filled glovebox with integrated vacuum chambers for the deposition of the solar cells components. Organic semiconductors, perovskites, MoO_3 and Au, were deposited in three different chambers, evacuated to a pressure of 10^{-6} mbar. MoO_3 was deposited at a rate of 0.1 Å/s to a thickness of 5 nm, and coated with TaTm (10 nm, deposited at 0.5 Å/s). The bilayer was annealed at 140 °C for 10 minutes. The $CsPbBrI_2$ perovskite films were fabricated following the procedures described above and coated with C60 (25 nm) and BCP (8 nm). Finally, a Ag electrode (100 nm) was deposited through a shadow mask to define the device layout (active area 2.1 x 3.1 mm^2).

Electrical Characterization. EQE was estimated by measuring the cell response at different wavelengths obtained with a white halogen lamp combined with band-pass filters. The solar spectrum was corrected by calibration with a silicon reference cell, previously calibrated (MiniSun simulator by ECN, the Netherlands). The current density voltage (J–V) characteristics were obtained using a solar simulator by Abet Technologies, model 10500, with an AM1.5G xenon lamp as the light source and a Keithley 2400 source measure unit. A shadow mask with an aperture of (2.2 x 1.2 mm^2) was used to precisely estimate the current density.

Structural Analysis. The crystalline structure of the powder and film samples was studied by X-ray diffraction (XRD). The patterns were collected in Bragg-Brentano geometry on an Empyrean PANalytical powder diffractometer with a copper anode operated at 45 kV and 40 mA. Further analysis including Le Bail fits were performed with Fullprof software. A scanning electron microscope (SEM) Hitachi S-4800 operating at 20 kV accelerating voltage was used to obtain SEM images. Samples were platinum-metallized prior to their observation. AFM measurements are collected in a Multimode atomic force microscope (Veeco instruments, Inc.). The images are obtained with a Si tip (frequency and K of ca. 320 kHz and 42 $N \cdot m^{-1}$, respectively) using the tapping-mode in air at room temperature. Images are recorded with a 0.5-1 Hz scan rate.

Optical Analysis. UV−vis absorption spectra were collected by using a fiber-optic Avantes Avaspec2048 spectrometer. The photoluminescence characteristics were studied using a Hyperspectral Imager IMA VIS from Photon Etc, coupled to a continuous-wave laser of 532 nm. The power density at the sample was set to AM1.5G 1 sun equivalence (41 mW/cm^2). For the analysis, the exposure time was set to 0.5 seconds and the area of the field of view measured was 333x333 μm. The spectrum was obtained by averaging the spectra of each pixel.

Sensitive EQE Analysis. For the sensitive EQE measurements, the cell was illuminated by a Quartz-Tungsten-Halogen lamp (Newport Apex 2-QTH) through a monochromator (Newport CS130-USB-3-MC), a chopper at 279 Hz and a focusing lens. The device current was measured as a function of energy from 2.1 eV to 1.2 eV in 0.02 eV steps using a lock-in amplifier (Stanford Research Systems SR830). The system was calibrated and the solar spectrum mismatch was corrected using a calibrated Silicon reference cell.

SUPPORTING INFORMATION

XRD analysis of powders and lattice parameters for all compounds. Additional optical absorption spectra, XRD of all precursors, additional thin film characterization (AFM, SEM, XPS), PV characterization of annealed devices, intensity dependent V_{oc} and J_{sc}, hyperspectral imaging and sensitive EQE of best samples.

Notes

The authors declare no competing financial interest.

ACKNOWLEDGMENTS

The research leading to these results has received funding from the European Research Council (ERC) under the European Union's Horizon 2020 research and innovation programme (Grant agreement No. 834431), the Spanish Ministry of Science, Innovation and Universities (MAT2017-88821-R, RTI2018-095362-A-I00, PCI2019-111829-2 and EQC2018-004888-P), the Comunitat Valenciana, IDIFEDER/2018/061 and the support of a fellowship from "la Caixa" Foundation (ID 100010434). The fellowship code is LCF/BQ/DI19/11730020. M.S. acknowledges the Spanish Ministry for his RyC contract.

REFERENCES

(1) Kojima, A.; Teshima, K.; Shirai, Y.; Miyasaka, T. Organometal Halide Perovskites as Visible-Light Sensitizers for Photovoltaic Cells. *J. Am. Chem. Soc.* **2009**, *131* (17), 6050–6051. https://doi.org/10.1021/ja809598r.

(2) Green, M. A.; Dunlop, E. D.; Hohl-Ebinger, J.; Yoshita, M.; Kopidakis, N.; Ho-Baillie, A. W. Y. Solar Cell Efficiency Tables (Version 55). *Prog. Photovoltaics Res. Appl.* **2020**, *28* (1), 3–15. https://doi.org/10.1002/pip.3228.

(3) Yang, W. S.; Park, B.-W.; Jung, E. H.; Jeon, N. J.; Kim, Y. C.; Lee, D. U.; Shin, S. S.; Seo, J.; Kim, E. K.; Noh, J. H.; et al. Iodide Management in Formamidinium-Lead-Halide–Based Perovskite Layers for Efficient Solar Cells. *Science (80-.).* **2017**, *356* (6345), 1376–1379. https://doi.org/10.1126/science.aan2301.

(4) Jeon, N. J.; Noh, J. H.; Yang, W. S.; Kim, Y. C.; Ryu, S.; Seo, J.; Seok, S. Il. Compositional Engineering of Perovskite Materials for High-Performance Solar Cells. *Nature* **2015**, *517* (7535), 476–480. https://doi.org/10.1038/nature14133.

(5) Saliba, M.; Matsui, T.; Seo, J.-Y.; Domanski, K.; Correa-Baena, J.-P.; Nazeeruddin, M. K.; Zakeeruddin, S. M.; Tress, W.; Abate, A.; Hagfeldt, A.; et al. Cesium-Containing Triple Cation Perovskite Solar Cells: Improved Stability, Reproducibility and High Efficiency. *Energy Environ. Sci.* **2016**, *9* (6), 1989–1997. https://doi.org/10.1039/C5EE03874J.

(6) Tan, H.; Jain, A.; Voznyy, O.; Lan, X.; García de Arquer, F. P.; Fan, J. Z.; Quintero-Bermudez, R.; Yuan, M.; Zhang, B.; Zhao, Y.; et al. Efficient and Stable Solution-Processed Planar Perovskite Solar Cells via Contact Passivation. *Science (80-.).* **2017**, *355* (6326), 722–726. https://doi.org/10.1126/science.aai9081.

(7) Turren-Cruz, S.-H.; Hagfeldt, A.; Saliba, M. Methylammonium-Free, High-Performance, and

Stable Perovskite Solar Cells on a Planar Architecture. *Science (80-.).* **2018**, *362* (6413), 449–453. https://doi.org/10.1126/science.aat3583.

(8) Liang, J.; Zhao, P.; Wang, C.; Wang, Y.; Hu, Y.; Zhu, G.; Ma, L.; Liu, J.; Jin, Z. $CsPb_{0.9}Sn_{0.1}IBr_2$ Based All-Inorganic Perovskite Solar Cells with Exceptional Efficiency and Stability. *J. Am. Chem. Soc.* **2017**, *139* (40), 14009–14012. https://doi.org/10.1021/jacs.7b07949.

(9) Wang, Y.; Zhang, T.; Kan, M.; Li, Y.; Wang, T.; Zhao, Y. Efficient α-$CsPbI_3$ Photovoltaics with Surface Terminated Organic Cations. *Joule* **2018**, *2* (10), 2065–2075. https://doi.org/10.1016/j.joule.2018.06.013.

(10) Liu, C.; Li, W.; Li, H.; Wang, H.; Zhang, C.; Yang, Y.; Gao, X.; Xue, Q.; Yip, H. L.; Fan, J.; et al. Structurally Reconstructed $CsPbI_2Br$ Perovskite for Highly Stable and Square-Centimeter All-Inorganic Perovskite Solar Cells. *Adv. Energy Mater.* **2019**, *9* (7), 1803572. https://doi.org/10.1002/aenm.201803572.

(11) Beal, R. E.; Slotcavage, D. J.; Leijtens, T.; Bowring, A. R.; Belisle, R. A.; Nguyen, W. H.; Burkhard, G. F.; Hoke, E. T.; McGehee, M. D. Cesium Lead Halide Perovskites with Improved Stability for Tandem Solar Cells. *J. Phys. Chem. Lett.* **2016**, *7* (5), 746–751. https://doi.org/10.1021/acs.jpclett.6b00002.

(12) Zeng, Q.; Zhang, X.; Liu, C.; Feng, T.; Chen, Z.; Zhang, W.; Zheng, W.; Zhang, H.; Yang, B. Inorganic $CsPbI_2Br$ Perovskite Solar Cells: The Progress and Perspective. *Sol. RRL* **2019**, *3* (1), 1800239. https://doi.org/10.1002/solr.201800239.

(13) Faheem, M. B.; Khan, B.; Feng, C.; Farooq, M. U.; Raziq, F.; Xiao, Y.; Li, Y. All-Inorganic Perovskite Solar Cells: Energetics, Key Challenges, and Strategies toward Commercialization. *ACS Energy Lett.* **2019**, 290–320. https://doi.org/10.1021/acsenergylett.9b02338.

(14) Li, X.; Wu, J.; Wang, S.; Qi, Y. Progress of All-Inorganic Cesium Lead-Free Perovskite Solar Cells. *Chem. Lett.* **2019**, *48* (8), 989–1005. https://doi.org/10.1246/cl.190270.

(15) Ho-Baillie, A.; Zhang, M.; Lau, C. F. J.; Ma, F.-J.; Huang, S. Untapped Potentials of Inorganic Metal Halide Perovskite Solar Cells. *Joule* **2019**, *3* (4), 938–955. https://doi.org/10.1016/j.joule.2019.02.002.

(16) Xiang, W.; Tress, W. Review on Recent Progress of All-Inorganic Metal Halide Perovskites and Solar Cells. *Adv. Mater.* **2019**, *31* (44), 1902851. https://doi.org/10.1002/adma.201902851.

(17) Tai, Q.; Tang, K.-C.; Yan, F. Recent Progress of Inorganic Perovskite Solar Cells. *Energy Environ.*

Sci. **2019**, *12* (8), 2375–2405. https://doi.org/10.1039/C9EE01479A.

(18) Wang, Y.; Dar, M. I.; Ono, L. K.; Zhang, T.; Kan, M.; Li, Y.; Zhang, L.; Wang, X.; Yang, Y.; Gao, X.; et al. Thermodynamically Stabilized β-$CsPbI_3$ –Based Perovskite Solar Cells with Efficiencies >18%. *Science (80-.).* **2019**, *365* (6453), 591–595. https://doi.org/10.1126/science.aav8680.

(19) Zheng, Y.; Yang, X.; Su, R.; Wu, P.; Gong, Q.; Zhu, R. High-Performance $CsPbI_xBr_{3-x}$ All-Inorganic Perovskite Solar Cells with Efficiency over 18% via Spontaneous Interfacial Manipulation. *Adv. Funct. Mater.* **2020**, *2000457*, 2000457. https://doi.org/10.1002/adfm.202000457.

(20) Han, Y.; Zhao, H.; Duan, C.; Yang, S.; Yang, Z.; Liu, Z.; Liu, S. Controlled N-Doping in Air-Stable $CsPbI_2Br$ Perovskite Solar Cells with a Record Efficiency of 16.79%. *Adv. Funct. Mater.* **2020**, *1909972*, 1–8. https://doi.org/10.1002/adfm.201909972.

(21) Zhang, Y.; Wu, C.; Wang, D.; Zhang, Z.; Qi, X.; Zhu, N.; Liu, G.; Li, X.; Hu, H.; Chen, Z.; et al. High Efficiency (16.37%) of Cesium Bromide—Passivated All-Inorganic $CsPbI_2Br$ Perovskite Solar Cells. *Sol. RRL* **2019**, *1900254*, 1900254. https://doi.org/10.1002/solr.201900254.

(22) Eperon, G. E.; Paternò, G. M.; Sutton, R. J.; Zampetti, A.; Haghighirad, A. A.; Cacialli, F.; Snaith, H. J. Inorganic Caesium Lead Iodide Perovskite Solar Cells. *J. Mater. Chem. A* **2015**, *3* (39), 19688–19695. https://doi.org/10.1039/C5TA06398A.

(23) Dastidar, S.; Hawley, C. J.; Dillon, A. D.; Gutierrez-Perez, A. D.; Spanier, J. E.; Fafarman, A. T. Quantitative Phase-Change Thermodynamics and Metastability of Perovskite-Phase Cesium Lead Iodide. *J. Phys. Chem. Lett.* **2017**, *8* (6), 1278–1282. https://doi.org/10.1021/acs.jpclett.7b00134.

(24) Wang, P.; Zhang, X.; Zhou, Y.; Jiang, Q.; Ye, Q.; Chu, Z.; Li, X.; Yang, X.; Yin, Z.; You, J. Solvent-Controlled Growth of Inorganic Perovskite Films in Dry Environment for Efficient and Stable Solar Cells. *Nat. Commun.* **2018**, *9* (1), 1–7. https://doi.org/10.1038/s41467-018-04636-4.

(25) Sutton, R. J.; Eperon, G. E.; Miranda, L.; Parrott, E. S.; Kamino, B. A.; Patel, J. B.; Hörantner, M. T.; Johnston, M. B.; Haghighirad, A. A.; Moore, D. T.; et al. Bandgap-Tunable Cesium Lead Halide Perovskites with High Thermal Stability for Efficient Solar Cells. *Adv. Energy Mater.* **2016**, *6* (8), 1502458. https://doi.org/10.1002/aenm.201502458.

(26) Tao, S.; Schmidt, I.; Brocks, G.; Jiang, J.; Tranca, I.; Meerholz, K.; Olthof, S. Absolute Energy Level Positions in Tin- and Lead-Based Halide Perovskites. *Nat. Commun.* **2019**, *10* (1), 2560. https://doi.org/10.1038/s41467-019-10468-7.

(27) Sutton, R. J.; Eperon, G. E.; Miranda, L.; Parrott, E. S.; Kamino, B. A.; Patel, J. B.; Hörantner, M. T.; Johnston, M. B.; Haghighirad, A. A.; Moore, D. T.; et al. Bandgap-Tunable Cesium Lead Halide Perovskites with High Thermal Stability for Efficient Solar Cells. *Adv. Energy Mater.* **2016**, *6* (8), 1502458. https://doi.org/10.1002/aenm.201502458.

(28) W. Travis, E. N. K. Glover, H. Bronstein, D. O. Scanlonbc, R. G. P. On the Application of the Tolerance Factor to Inorganic and Hybrid Halide Perovskites : A Revised. *Chem. Sci.* **2016**, *7*, 4548–4556. https://doi.org/10.1039/c5sc04845a.

(29) Nam, J. K.; Chai, S. U.; Cha, W.; Choi, Y. J.; Kim, W.; Jung, M. S.; Kwon, J.; Kim, D.; Park, J. H. Potassium Incorporation for Enhanced Performance and Stability of Fully Inorganic Cesium Lead Halide Perovskite Solar Cells. *Nano Lett.* **2017**, *17* (3), 2028–2033. https://doi.org/10.1021/acs.nanolett.7b00050.

(30) Han, Y.; Zhao, H.; Duan, C.; Yang, S.; Yang, Z.; Liu, Z.; Liu, S. (Frank). Controlled N-Doping in Air-Stable $CsPbI_2Br$ Perovskite Solar Cells with a Record Efficiency of 16.79%. *Adv. Funct. Mater.* **2020**, *30* (12), 1909972. https://doi.org/10.1002/adfm.201909972.

(31) Lau, C. F. J.; Zhang, M.; Deng, X.; Zheng, J.; Bing, J.; Ma, Q.; Kim, J.; Hu, L.; Green, M. A.; Huang, S.; et al. Strontium-Doped Low-Temperature-Processed $CsPbI_2Br$ Perovskite Solar Cells. *ACS Energy Lett.* **2017**, *2* (10), 2319–2325. https://doi.org/10.1021/acsenergylett.7b00751.

(32) Xiang, W.; Wang, Z.; Kubicki, D. J.; Wang, X.; Tress, W.; Luo, J.; Zhang, J.; Hofstetter, A.; Zhang, L.; Emsley, L.; et al. Ba-Induced Phase Segregation and Band Gap Reduction in Mixed-Halide Inorganic Perovskite Solar Cells. *Nat. Commun.* **2019**, *10* (1), 4686. https://doi.org/10.1038/s41467-019-12678-5.

(33) Mali, S. S.; Patil, J. V.; Hong, C. K. Hot-Air-Assisted Fully Air-Processed Barium Incorporated $CsPbI_2Br$ Perovskite Thin Films for Highly Efficient and Stable All-Inorganic Perovskite Solar Cells. *Nano Lett.* **2019**, *19* (9), 6213–6220. https://doi.org/10.1021/acs.nanolett.9b02277.

(34) Wang, K.-L.; Wang, R.; Wang, Z.-K.; Li, M.; Zhang, Y.; Ma, H.; Liao, L.-S.; Yang, Y. Tailored Phase Transformation of $CsPbI_2Br$ Films by Copper(II) Bromide for High-Performance All-Inorganic Perovskite Solar Cells. *Nano Lett.* **2019**, *19* (8), 5176–5184. https://doi.org/10.1021/acs.nanolett.9b01553.

(35) Sun, H.; Zhang, J.; Gan, X.; Yu, L.; Yuan, H.; Shang, M.; Lu, C.; Hou, D.; Hu, Z.; Zhu, Y.; et al. Pb-Reduced $CsPb_{0.9}Zn_{0.1}I_2Br$ Thin Films for Efficient Perovskite Solar Cells. *Adv. Energy Mater.* **2019**, *9* (25), 1900896. https://doi.org/10.1002/aenm.201900896.

(36) Chen, L.; Wan, L.; Li, X.; Zhang, W.; Fu, S.; Wang, Y.; Li, S.; Wang, H.-Q.; Song, W.; Fang, J. Inverted All-Inorganic $CsPbI_2Br$ Perovskite Solar Cells with Promoted Efficiency and Stability by Nickel Incorporation. *Chem. Mater.* **2019**, *31* (21), 9032–9039. https://doi.org/10.1021/acs.chemmater.9b03277.

(37) Mali, S. S.; Patil, J. V.; Hong, C. K. Simultaneous Improved Performance and Thermal Stability of Planar Metal Ion Incorporated $CsPbI_2Br$ All-Inorganic Perovskite Solar Cells Based on MgZnO Nanocrystalline Electron Transporting Layer. *Adv. Energy Mater.* **2020**, *10* (3), 1902708. https://doi.org/10.1002/aenm.201902708.

(38) Bai, D.; Zhang, J.; Jin, Z.; Bian, H.; Wang, K.; Wang, H.; Liang, L.; Wang, Q.; Liu, S. F. Interstitial Mn^{2+} -Driven High-Aspect-Ratio Grain Growth for Low-Trap-Density Microcrystalline Films for Record Efficiency $CsPbI_2Br$ Solar Cells. *ACS Energy Lett.* **2018**, *3* (4), 970–978. https://doi.org/10.1021/acsenergylett.8b00270.

(39) Ye, L.; Wang, H.; Wei, Y.; Guo, P.; Yang, X.; Ye, Q.; Wang, H. Acetate-Based Crystallization Kinetics Modulation of $CsPbI_2Br$ for Improved Photovoltaic Performance. *ACS Appl. Energy Mater.* **2020**, *3* (1), 658–665. https://doi.org/10.1021/acsaem.9b01859.

(40) Xiang, W.; Wang, Z.; Kubicki, D. J.; Tress, W.; Luo, J.; Prochowicz, D.; Akin, S.; Emsley, L.; Zhou, J.; Dietler, G.; et al. Europium-Doped $CsPbI_2Br$ for Stable and Highly Efficient Inorganic Perovskite Solar Cells. *Joule* **2019**, *3* (1), 205–214. https://doi.org/10.1016/j.joule.2018.10.008.

(41) Shi, J.; Li, F.; Yuan, J.; Ling, X.; Zhou, S.; Qian, Y.; Ma, W. Efficient and Stable $CsPbI_3$ Perovskite Quantum Dots Enabled by in Situ Ytterbium Doping for Photovoltaic Applications. *J. Mater. Chem. A* **2019**, *7* (36), 20936–20944. https://doi.org/10.1039/C9TA07143A.

(42) Yang, S.; Zhao, H.; Han, Y.; Duan, C.; Liu, Z.; Liu, S. (Frank). Europium and Acetate Co-doping Strategy for Developing Stable and Efficient CsPbI 2 Br Perovskite Solar Cells. *Small* **2019**, *15* (46), 1904387. https://doi.org/10.1002/smll.201904387.

(43) Xu, W.; He, F.; Zhang, M.; Nie, P.; Zhang, S.; Zhao, C.; Luo, R.; Li, J.; Zhang, X.; Zhao, S.; et al. Minimizing Voltage Loss in Efficient All-Inorganic $CsPbI_2Br$ Perovskite Solar Cells through Energy Level Alignment. *ACS Energy Lett.* **2019**, *4* (10), 2491–2499. https://doi.org/10.1021/acsenergylett.9b01662.

(44) Chen, W.; Chen, H.; Xu, G.; Xue, R.; Wang, S.; Li, Y.; Li, Y. Precise Control of Crystal Growth for Highly Efficient $CsPbI_2Br$ Perovskite Solar Cells. *Joule* **2019**, *3* (1), 191–204. https://doi.org/10.1016/j.joule.2018.10.011.

(45) Shao, Z.; Wang, Z.; Li, Z.; Fan, Y.; Meng, H.; Liu, R.; Wang, Y.; Hagfeldt, A.; Cui, G.; Pang, S. A Scalable Methylamine Gas Healing Strategy for High-Efficiency Inorganic Perovskite Solar Cells. *Angew. Chemie Int. Ed.* **2019**, *58* (17), 5587–5591. https://doi.org/10.1002/anie.201814024.

(46) Zhao, H.; Han, Y.; Xu, Z.; Duan, C.; Yang, S.; Yuan, S.; Yang, Z.; Liu, Z.; Liu, S. (Frank). A Novel Anion Doping for Stable $CsPbI_2Br$ Perovskite Solar Cells with an Efficiency of 15.56% and an Open Circuit Voltage of 1.30 V. *Adv. Energy Mater.* **2019**, *9* (40), 1902279. https://doi.org/10.1002/aenm.201902279.

(47) Ma, J.; Qin, M.; Li, Y.; Zhang, T.; Xu, J.; Fang, G.; Lu, X. Guanidinium Doping Enabled Low-Temperature Fabrication of High-Efficiency All-Inorganic $CsPbI_2Br$ Perovskite Solar Cells. *J. Mater. Chem. A* **2019**, *7* (48), 27640–27647. https://doi.org/10.1039/C9TA10899H.

(48) Jiang, H.; Feng, J.; Zhao, H.; Li, G.; Yin, G.; Han, Y.; Yan, F.; Liu, Z.; Liu, S. (Frank). Low Temperature Fabrication for High Performance Flexible $CsPbI_2Br$ Perovskite Solar Cells. *Adv. Sci.* **2018**, *5* (11), 1801117. https://doi.org/10.1002/advs.201801117.

(49) Yang, X.; Yang, H.; Hu, X.; Li, W.; Fang, Z.; Zhang, K.; Huang, R.; Li, J.; Yang, Z.; Song, Y. Low-Temperature Interfacial Engineering for Flexible $CsPbI_2Br$ Perovskite Solar Cells with High Performance beyond 15%. *J. Mater. Chem. A* **2020**, *8* (10), 5308–5314. https://doi.org/10.1039/C9TA13922B.

(50) Liu, C.; Yang, Y.; Zhang, C.; Wu, S.; Wei, L.; Guo, F.; Arumugam, G. M.; Hu, J.; Liu, X.; Lin, J.; et al. Tailoring C 60 for Efficient Inorganic $CsPbI_2Br$ Perovskite Solar Cells and Modules. *Adv. Mater.* **2020**, *32* (8), 1907361. https://doi.org/10.1002/adma.201907361.

(51) Yan, L.; Xue, Q.; Liu, M.; Zhu, Z.; Tian, J.; Li, Z.; Chen, Z.; Chen, Z.; Yan, H.; Yip, H.-L.; et al. Interface Engineering for All-Inorganic $CsPbI_2Br$ Perovskite Solar Cells with Efficiency over 14%. *Adv. Mater.* **2018**, *30* (33), 1802509. https://doi.org/10.1002/adma.201802509.

(52) Liu, C.; Li, W.; Zhang, C.; Ma, Y.; Fan, J.; Mai, Y. All-Inorganic $CsPbI_2Br$ Perovskite Solar Cells with High Efficiency Exceeding 13%. *J. Am. Chem. Soc.* **2018**, *140* (11), 3825–3828. https://doi.org/10.1021/jacs.7b13229.

(53) Ma, J.; Su, J.; Lin, Z.; Zhou, L.; He, J.; Zhang, J.; Liu, S.; Chang, J.; Hao, Y. Improve the Oxide/Perovskite Heterojunction Contact for Low Temperature High Efficiency and Stable All-Inorganic CsPbI2Br Perovskite Solar Cells. *Nano Energy* **2020**, *67* (September 2019), 104241. https://doi.org/10.1016/j.nanoen.2019.104241.

(54) Shen, E.; Chen, J.; Tian, Y.; Luo, Y.; Shen, Y.; Sun, Q.; Jin, T.; Shi, G.; Li, Y.; Tang, J. Interfacial Energy Level Tuning for Efficient and Thermostable CsPbI 2 Br Perovskite Solar Cells. *Adv. Sci.* **2020**, *7* (1), 1901952. https://doi.org/10.1002/advs.201901952.

(55) Jiang, K.; Wang, J.; Wu, F.; Xue, Q.; Yao, Q.; Zhang, J.; Chen, Y.; Zhang, G.; Zhu, Z.; Yan, H.; et al. Dopant-Free Organic Hole- Transporting Material for Efficient and Stable Inverted All-Inorganic and Hybrid Perovskite Solar Cells. *Adv. Mater.* **2020**, *1908011*, 1908011. https://doi.org/10.1002/adma.201908011.

(56) Xiao, Q.; Tian, J.; Xue, Q.; Wang, J.; Xiong, B.; Han, M.; Li, Z.; Zhu, Z.; Yip, H.; Li, Z. Dopant-Free Squaraine-Based Polymeric Hole- Transporting Materials with Comprehensive Passivation Effects for Efficient All-Inorganic Perovskite Solar Cells. *Angew. Chemie Int. Ed.* **2019**, *58* (49), 17724–17730. https://doi.org/10.1002/anie.201907331.

(57) Zhao, H.; Yang, S.; Han, Y.; Yuan, S.; Jiang, H.; Duan, C.; Liu, Z.; Liu, S. (Frank). A High Mobility Conjugated Polymer Enables Air and Thermally Stable $CsPbI_2Br$ Perovskite Solar Cells with an Efficiency Exceeding 15%. *Adv. Mater. Technol.* **2019**, *4* (9), 1900311. https://doi.org/10.1002/admt.201900311.

(58) Tian, J.; Xue, Q.; Tang, X.; Chen, Y.; Li, N.; Hu, Z.; Shi, T.; Wang, X.; Huang, F.; Brabec, C. J.; et al. Dual Interfacial Design for Efficient $CsPbI_2Br$ Perovskite Solar Cells with Improved Photostability. *Adv. Mater.* **2019**, *31* (23), 1901152. https://doi.org/10.1002/adma.201901152.

(59) Liu, M.; Johnston, M. B.; Snaith, H. J. Efficient Planar Heterojunction Perovskite Solar Cells by Vapour Deposition. *Nature* **2013**, *501* (7467), 395–398. https://doi.org/10.1038/nature12509.

(60) Ávila, J.; Momblona, C.; Boix, P. P.; Sessolo, M.; Bolink, H. J. Vapor-Deposited Perovskites: The Route to High-Performance Solar Cell Production? *Joule* **2017**, *1* (3), 431–442. https://doi.org/10.1016/j.joule.2017.07.014.

(61) Forgács, D.; Gil-Escrig, L.; Pérez-Del-Rey, D.; Momblona, C.; Werner, J.; Niesen, B.; Ballif, C.; Sessolo, M.; Bolink, H. J. Efficient Monolithic Perovskite/Perovskite Tandem Solar Cells. *Adv. Energy Mater.* **2017**, *7* (8), 1602121. https://doi.org/10.1002/aenm.201602121.

(62) Ávila, J.; Momblona, C.; Boix, P.; Sessolo, M.; Anaya, M.; Lozano, G.; Vandewal, K.; Míguez, H.; Bolink, H. J. High Voltage Vacuum-Deposited $CH_3NH_3PbI_3$–$CH_3NH_3PbI_3$ Tandem Solar Cells. *Energy Environ. Sci.* **2018**, *11* (11), 3292–3297. https://doi.org/10.1039/C8EE01936C.

(63) Sahli, F.; Werner, J.; Kamino, B. A.; Bräuninger, M.; Monnard, R.; Paviet-Salomon, B.; Barraud,

L.; Ding, L.; Diaz Leon, J. J.; Sacchetto, D.; et al. Fully Textured Monolithic Perovskite/Silicon Tandem Solar Cells with 25.2% Power Conversion Efficiency. *Nat. Mater.* **2018**, *17* (9), 820–826. https://doi.org/10.1038/s41563-018-0115-4.

(64) Malinkiewicz, O.; Yella, A.; Lee, Y. H.; Espallargas, G. M.; Graetzel, M.; Nazeeruddin, M. K.; Bolink, H. J. Perovskite Solar Cells Employing Organic Charge-Transport Layers. *Nat. Photonics* **2014**, *8* (2), 128–132. https://doi.org/10.1038/nphoton.2013.341.

(65) Lin, Q.; Armin, A.; Nagiri, R. C. R.; Burn, P. L.; Meredith, P. Electro-Optics of Perovskite Solar Cells. *Nat. Photonics* **2015**, *9* (2), 106–112. https://doi.org/10.1038/nphoton.2014.284.

(66) Chirvony, V. S.; Sekerbayev, K. S.; Pérez-del-Rey, D.; Martínez-Pastor, J. P.; Palazon, F.; Boix, P. P.; Taurbayev, T. I.; Sessolo, M.; Bolink, H. J. Short Photoluminescence Lifetimes in Vacuum-Deposited $CH_3NH_3PbI_3$ Perovskite Thin Films as a Result of Fast Diffusion of Photogenerated Charge Carriers. *J. Phys. Chem. Lett.* **2019**, *10* (17), 5167–5172. https://doi.org/10.1021/acs.jpclett.9b02329.

(67) Patel, J. B.; Wright, A. D.; Lohmann, K. B.; Peng, K.; Xia, C. Q.; Ball, J. M.; Noel, N. K.; Crothers, T. W.; Wong-Leung, J.; Snaith, H. J.; et al. Light Absorption and Recycling in Hybrid Metal Halide Perovskite Photovoltaic Devices. *Adv. Energy Mater.* **2020**, *10* (10), 1903653. https://doi.org/10.1002/aenm.201903653.

(68) Longo, G.; Momblona, C.; La-Placa, M.-G.; Gil-Escrig, L.; Sessolo, M.; Bolink, H. J. Fully Vacuum-Processed Wide Band Gap Mixed-Halide Perovskite Solar Cells. *ACS Energy Lett.* **2018**, *3* (1), 214–219. https://doi.org/10.1021/acsenergylett.7b01217.

(69) Gil-Escrig, L.; Momblona, C.; La-Placa, M.-G.; Boix, P. P.; Sessolo, M.; Bolink, H. J. Vacuum Deposited Triple-Cation Mixed-Halide Perovskite Solar Cells. *Adv. Energy Mater.* **2018**, *8* (14), 1703506. https://doi.org/10.1002/aenm.201703506.

(70) Babaei, A.; Soltanpoor, W.; Tesa-Serrate, M. A.; Yerci, S.; Sessolo, M.; Bolink, H. J. Preparation and Characterization of Mixed Halide $MAPbI_{3-x}Cl_x$ Perovskite Thin Films by Three-Source Vacuum Deposition. *Energy Technol.* **2019**, 1900784. https://doi.org/10.1002/ente.201900784.

(71) Igual-Muñoz, A. M.; Castillo, A.; Dreessen, C.; Boix, P. P.; Bolink, H. J. Vacuum-Deposited Multication Tin–Lead Perovskite Solar Cells. *ACS Appl. Energy Mater.* **2020**, *3* (3), 2755–2761. https://doi.org/10.1021/acsaem.9b02413.

(72) Burwig, T.; Fränzel, W.; Pistor, P. Crystal Phases and Thermal Stability of Co-Evaporated $CsPbX_3$

(X = I, Br) Thin Films. *J. Phys. Chem. Lett.* **2018**, *9* (16), 4808–4813. https://doi.org/10.1021/acs.jpclett.8b02059.

(73) Palazon, F.; Pérez-del-Rey, D.; Dänekamp, B.; Dreessen, C.; Sessolo, M.; Boix, P. P.; Bolink, H. J. Room-Temperature Cubic Phase Crystallization and High Stability of Vacuum-Deposited Methylammonium Lead Triiodide Thin Films for High-Efficiency Solar Cells. *Adv. Mater.* **2019**, *31* (39), 1902692. https://doi.org/10.1002/adma.201902692.

(74) Lohmann, K. B.; Patel, J. B.; Rothmann, M. U.; Xia, C. Q.; Oliver, R. D. J.; Herz, L. M.; Snaith, H. J.; Johnston, M. B. Control over Crystal Size in Vapor Deposited Metal-Halide Perovskite Films. *ACS Energy Lett.* **2020**, *5* (3), 710–717. https://doi.org/10.1021/acsenergylett.0c00183.

(75) Shahiduzzaman, M.; Yonezawa, K.; Yamamoto, K.; Ripolles, T. S.; Karakawa, M.; Kuwabara, T.; Takahashi, K.; Hayase, S.; Taima, T. Improved Reproducibility and Intercalation Control of Efficient Planar Inorganic Perovskite Solar Cells by Simple Alternate Vacuum Deposition of PbI_2 and CsI. *ACS Omega* **2017**, *2* (8), 4464–4469. https://doi.org/10.1021/acsomega.7b00814.

(76) Kottokkaran, R.; Gaonkar, H. A.; Bagheri, B.; Dalal, V. L. Efficient P-i-n Inorganic $CsPbI_3$ Perovskite Solar Cell Deposited Using Layer-by-Layer Vacuum Deposition. *J. Vac. Sci. Technol. A* **2018**, *36* (4), 041201. https://doi.org/10.1116/1.5029253.

(77) Frolova, L. A.; Anokhin, D. V.; Piryazev, A. A.; Luchkin, S. Y.; Dremova, N. N.; Stevenson, K. J.; Troshin, P. A. Highly Efficient All-Inorganic Planar Heterojunction Perovskite Solar Cells Produced by Thermal Coevaporation of CsI and PbI_2. *J. Phys. Chem. Lett.* **2017**, *8* (1), 67–72. https://doi.org/10.1021/acs.jpclett.6b02594.

(78) Park, C.-G.; Choi, W.-G.; Na, S.; Moon, T. All-Inorganic Perovskite $CsPbI_2Br$ Through Co-Evaporation for Planar Heterojunction Solar Cells. *Electron. Mater. Lett.* **2019**, *15* (1), 56–60. https://doi.org/10.1007/s13391-018-0095-1.

(79) Chen, C.-Y.; Lin, H.-Y.; Chiang, K.-M.; Tsai, W.-L.; Huang, Y.-C.; Tsao, C.-S.; Lin, H.-W. All-Vacuum-Deposited Stoichiometrically Balanced Inorganic Cesium Lead Halide Perovskite Solar Cells with Stabilized Efficiency Exceeding 11%. *Adv. Mater.* **2017**, *29* (12), 1605290. https://doi.org/10.1002/adma.201605290.

(80) Becker, P.; Márquez, J. A.; Just, J.; Al-Ashouri, A.; Hages, C.; Hempel, H.; Jošt, M.; Albrecht, S.; Frahm, R.; Unold, T. Low Temperature Synthesis of Stable γ-$CsPbI_3$ Perovskite Layers for Solar Cells Obtained by High Throughput Experimentation. *Adv. Energy Mater.* **2019**, *9* (22), 1900555. https://doi.org/10.1002/aenm.201900555.

(81) Hutter, E. M.; Sutton, R. J.; Chandrashekar, S.; Abdi-Jalebi, M.; Stranks, S. D.; Snaith, H. J.; Savenije, T. J. Vapour-Deposited Cesium Lead Iodide Perovskites: Microsecond Charge Carrier Lifetimes and Enhanced Photovoltaic Performance. *ACS Energy Lett.* **2017**, *2* (8), 1901–1908. https://doi.org/10.1021/acsenergylett.7b00591.

(82) Lin, H.; Chen, C.; Hsu, B.; Cheng, Y.; Tsai, W.; Huang, Y.; Tsao, C.; Lin, H. Efficient Cesium Lead Halide Perovskite Solar Cells through Alternative Thousand-Layer Rapid Deposition. *Adv. Funct. Mater.* **2019**, *29* (44), 1905163. https://doi.org/10.1002/adfm.201905163.

(83) Yang, D.; Yang, R.; Priya, S.; Liu, S. (Frank). Recent Advances in Flexible Perovskite Solar Cells: Fabrication and Applications. *Angew. Chemie Int. Ed.* **2019**, *58* (14), 4466–4483. https://doi.org/10.1002/anie.201809781.

(84) Palazon, F.; El Ajjouri, Y.; Bolink, H. J. Making by Grinding: Mechanochemistry Boosts the Development of Halide Perovskites and Other Multinary Metal Halides. *Adv. Energy Mater.* **2019**, *10* (13), 1902499. https://doi.org/10.1002/aenm.201902499.

(85) El Ajjouri, Y.; Palazon, F.; Sessolo, M.; Bolink, H. J. Single-Source Vacuum Deposition of Mechanosynthesized Inorganic Halide Perovskites. *Chem. Mater.* **2018**, *30* (21), 7423–7427. https://doi.org/10.1021/acs.chemmater.8b03352.

(86) Akkerman, Q. A.; Manna, L. What Defines a Halide Perovskite? *ACS Energy Lett.* **2020**, *5* (2), 604–610. https://doi.org/10.1021/acsenergylett.0c00039.

(87) Karmakar, A.; Dodd, M. S.; Zhang, X.; Oakley, M. S.; Klobukowski, M.; Michaelis, V. K. Mechanochemical Synthesis of 0D and 3D Cesium Lead Mixed Halide Perovskites. *Chem. Commun.* **2019**, *55* (35), 5079–5082. https://doi.org/10.1039/C8CC09622H.

(88) Liu, Z.; Bekenstein, Y.; Ye, X.; Nguyen, S. C.; Swabeck, J.; Zhang, D.; Lee, S. T.; Yang, P.; Ma, W.; Alivisatos, A. P. Ligand Mediated Transformation of Cesium Lead Bromide Perovskite Nanocrystals to Lead Depleted Cs_4PbBr_6 Nanocrystals. *J. Am. Chem. Soc.* **2017**, *139* (15), 5309–5312. https://doi.org/10.1021/jacs.7b01409.

(89) Palazon, F.; Urso, C.; De Trizio, L.; Akkerman, Q.; Marras, S.; Locardi, F.; Nelli, I.; Ferretti, M.; Prato, M.; Manna, L. Postsynthesis Transformation of Insulating Cs_4PbBr_6 Nanocrystals into Bright Perovskite $CsPbBr_3$ through Physical and Chemical Extraction of CsBr. *ACS Energy Lett.* **2017**, *2* (10), 2445–2448. https://doi.org/10.1021/acsenergylett.7b00842.

(90) Palazon, F.; Almeida, G.; Akkerman, Q. A.; De Trizio, L.; Dang, Z.; Prato, M.; Manna, L. Changing

the Dimensionality of Cesium Lead Bromide Nanocrystals by Reversible Postsynthesis Transformations with Amines. *Chem. Mater.* **2017**, *29* (10), 4167–4171. https://doi.org/10.1021/acs.chemmater.7b00895.

(91) *CRC Handbook of Chemistry and Physics*, 100th ed.; Rumble, J. R., Ed.; Taylor & Francis Ltd; CRC Press, London, **2020**.

(92) Palazon, F.; El Ajjouri, Y.; Sebastia-Luna, P.; Lauciello, S.; Manna, L.; Bolink, H. J. Mechanochemical Synthesis of Inorganic Halide Perovskites: Evolution of Phase-Purity, Morphology, and Photoluminescence. *J. Mater. Chem. C* **2019**, *7* (37), 11406–11410. https://doi.org/10.1039/C9TC03778K.

(93) Burwig, T.; Fränzel, W.; Pistor, P. Crystal Phases and Thermal Stability of Co-Evaporated $CsPbX_3$ (X = I, Br) Thin Films. *J. Phys. Chem. Lett.* **2018**, *9* (16), 4808–4813. https://doi.org/10.1021/acs.jpclett.8b02059.

(94) Pistor, P.; Burwig, T.; Brzuska, C.; Weber, B.; Fränzel, W. Thermal Stability and Miscibility of Co-Evaporated Methyl Ammonium Lead Halide ($MAPbX_3$, X = I, Br, Cl) Thin Films Analysed by in Situ X-Ray Diffraction. *J. Mater. Chem. A* **2018**, *6* (24), 11496–11506. https://doi.org/10.1039/C8TA02775G.

(95) Mattox, D. M. Vacuum Evaporation and Vacuum Deposition. In *Handbook of Physical Vapor Deposition (PVD) Processing*; Mattox, D. M. B. T.-H. of P. V. D. (PVD) P. (Second E., Ed.; Elsevier: Boston, 2010; pp 195–235. https://doi.org/10.1016/B978-0-8155-2037-5.00006-X.

(96) Vapor Pressure Graphs for Inorganic Compounds and Elements. In *Inorganic Compounds and Elements*; Yaws, C. L. B. T.-H. of V. P., Ed.; Gulf Professional Publishing, 1995; Vol. 4, pp 1–343. https://doi.org/10.1016/S1874-8813(06)80004-1.

(97) Gil-Escrig, L.; Momblona, C.; La-Placa, M.-G.; Boix, P. P.; Sessolo, M.; Bolink, H. J. Vacuum Deposited Triple-Cation Mixed-Halide Perovskite Solar Cells. *Adv. Energy Mater.* **2018**, *8* (14), 1703506. https://doi.org/10.1002/aenm.201703506.

(98) Rühle, S. Tabulated Values of the Shockley–Queisser Limit for Single Junction Solar Cells. *Sol. Energy* **2016**, *130*, 139–147. https://doi.org/10.1016/j.solener.2016.02.015.

(99) Tvingstedt, K.; Malinkiewicz, O.; Baumann, A.; Deibel, C.; Snaith, H. J.; Dyakonov, V.; Bolink, H. J. Radiative Efficiency of Lead Iodide Based Perovskite Solar Cells. *Sci. Rep.* **2014**, *4*, 6071. https://doi.org/10.1038/srep06071.

(100) Rau, U.; Blank, B.; Müller, T. C. M.; Kirchartz, T. Efficiency Potential of Photovoltaic Materials and Devices Unveiled by Detailed-Balance Analysis. *Phys. Rev. Appl.* **2017**, *7* (4), 1–9. https://doi.org/10.1103/PhysRevApplied.7.044016.

(101) Shockley, W.; Queisser, H. J. Detailed Balance Limit of Efficiency of P-n Junction Solar Cells. *J. Appl. Phys.* **1961**, *32* (3), 510–519. https://doi.org/10.1063/1.1736034.

(102) Rühle, S. Tabulated Values of the Shockley-Queisser Limit for Single Junction Solar Cells. *Sol. Energy* **2016**, *130*, 139–147. https://doi.org/10.1016/j.solener.2016.02.015.

(103) Green, M. A. Solar Cell Fill Factors: General Graph and Empirical Expressions. *Solid State Electron.* **1981**, *24* (8), 788–789. https://doi.org/10.1016/0038-1101(81)90062-9.

(104) Jaysankar, M.; Raul, B. A. L.; Bastos, J.; Burgess, C.; Weijtens, C.; Creatore, M.; Aernouts, T.; Kuang, Y.; Gehlhaar, R.; Hadipour, A.; et al. Minimizing Voltage Loss in Wide-Bandgap Perovskites for Tandem Solar Cells. *ACS Energy Lett.* **2019**, *4* (1), 259–264. https://doi.org/10.1021/acsenergylett.8b02179.

(105) Burkhard, G. F.; Hoke, E. T.; Beiley, Z. M.; Mcgehee, M. D. Free Carrier Generation in Fullerene Acceptors and Its Effect on Polymer Photovoltaics. *J. Phys. Chem. C* **2012**, *116* (50), 26674–26678. https://doi.org/10.1021/jp310821f.

(106) Chantana, J.; Kawano, Y.; Nishimura, T.; Mavlonov, A.; Minemoto, T. Impact of Urbach Energy on Open-Circuit Voltage Deficit of Thin-Film Solar Cells. *Sol. Energy Mater. Sol. Cells* **2020**, *210* (January), 110502. https://doi.org/10.1016/j.solmat.2020.110502.

Supporting Information

Room temperature vacuum-deposition of $CsPbI_2Br$ perovskite films from multiple-sources and mixed halide precursors.

Ana M. Igual-Muñoz, Javier Navarro-Alapont, Chris Dreessen, Francisco Palazon, Michele Sessolo*, Henk J. Bolink

Instituto de Ciencia Molecular, Universidad de Valencia, C/ J. Beltran 2, 46980 Paterna, Spain.

*E-mail: michele.sessolo@uv.es

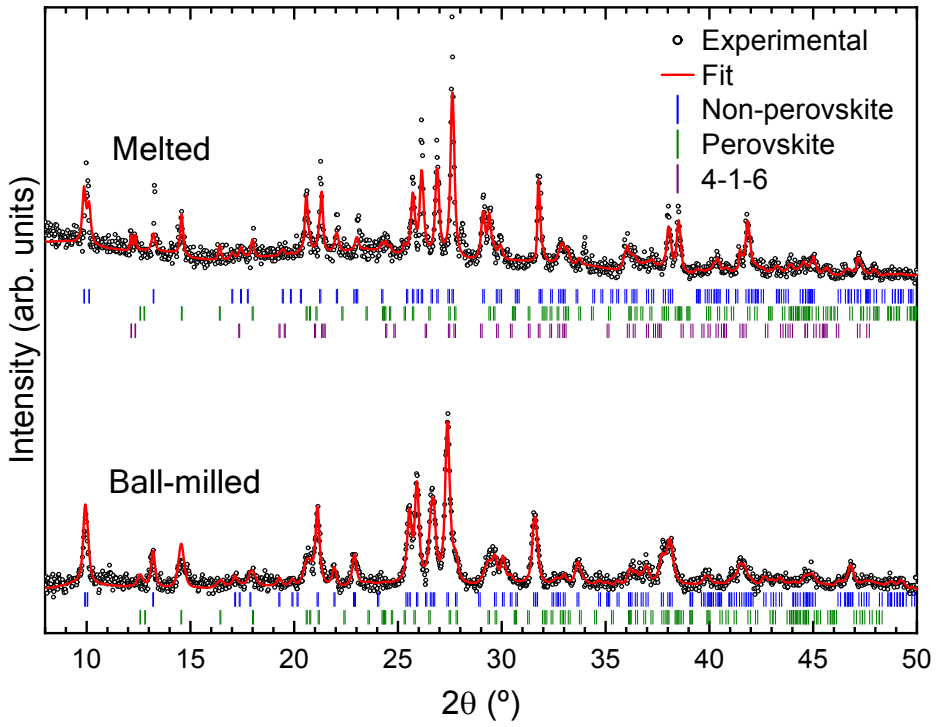

Figure S1. XRD characterization of ball-milled (bottom) and melted (top) CsBr:PbI_2 1:1 powders. Open circles represent raw data, red lines are whole-pattern Le Bail fit and vertical lines indicate the calculated Bragg's reflections for different phases. More details about the different phases in the discussion.

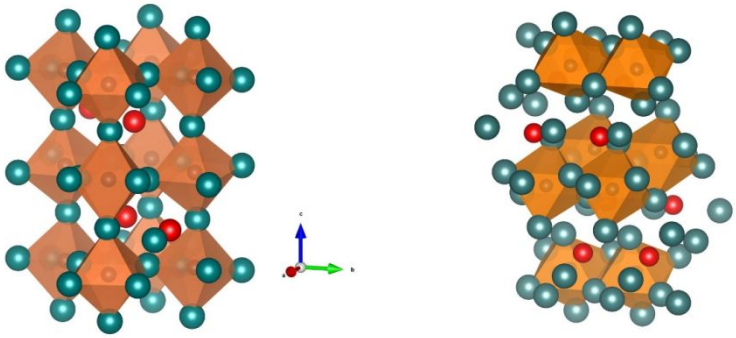

Figure S2. Crystal structures of the distorted perovskite and non-perovskite phases. Cs^+ ions are depicted in red, halide anions in teal, Pb^{2+} cations in grey and PbX_6 octahedra in orange.

Table S1. Lattice parameters for perovskite and non-perovskite phases of ball-milled and melted samples together with reference values for $CsPbBr_3$ and $CsPbI_3$ retrieved from the Inorganic Crystal Structure Database (references 97851 and 161480 respectively).

Ball-milled	*a (Å)*	*b (Å)*	*c (Å)*	*α*	*β*	*γ*	*Vol (Å³)*
Perovskite ($CsPbBr_3$)	8.392 (8.207)	8.624 (8.255)	12.168 (11.759)	90 (90)	90 (90)	90 (90)	880 (797)
Non-Perovskite ($CsPbI_3$)	10.341 (10.458)	4.770 (4.802)	17.621 (17.776)	90 (90)	90 (90)	90 (90)	869 (893)
Melted	*a (Å)*	*b (Å)*	*c (Å)*	*α*	*β*	*γ*	*Vol (Å³)*
Perovskite ($CsPbBr_3$)	8.435 (8.207)	8.629 (8.255)	12.151 (11.759)	90 (90)	90 (90)	90 (90)	880 (797)
Non-Perovskite ($CsPbI_3$)	10.424 (10.458)	4.730 (4.802)	17.486 (17.776)	90 (90)	90 (90)	90 (90)	869 (893)

Table S2. Lattice parameters calculated for thin-films deposited by different methods referred to the values for $CsPbBr_3$ retrieved from the Inorganic Crystal Structure Database (reference 97851).

	a (Å)	*b (Å)*	*c (Å)*	*α*	*β*	*γ*	*Vol (Å³)*
$CsPbBr_3$ (ICSD-97851)	8.207	8.255	11.759	90	90	90	797
2-sources	8.587	8.737	12.086	90	90	90	907
2-sources (MHP)	8.614	8.732	11.848	90	90	90	891
3-sources (slow)	8.627	8.746	12.136	90	90	90	916
3-sources (fast)	8.627	8.724	12.076	90	90	90	909
4-sources	8.573	8.725	12.068	90	90	90	903

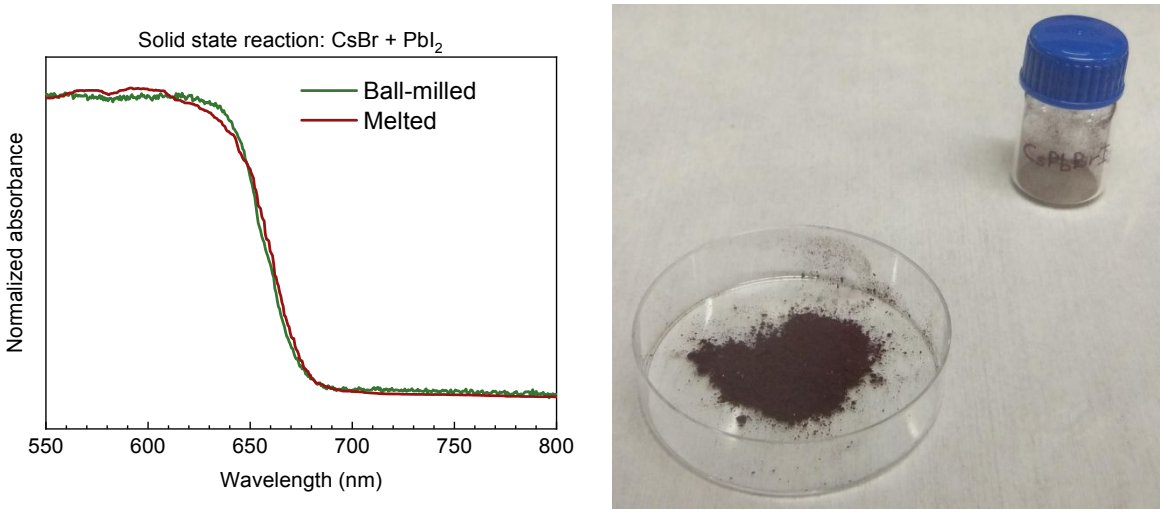

Figure S3. UV-Vis optical absorption for powders obtained by mechanochemical and melting techniques. A photograph of as-prepared perovskite from mechanochemical synthesis is shown as reference.

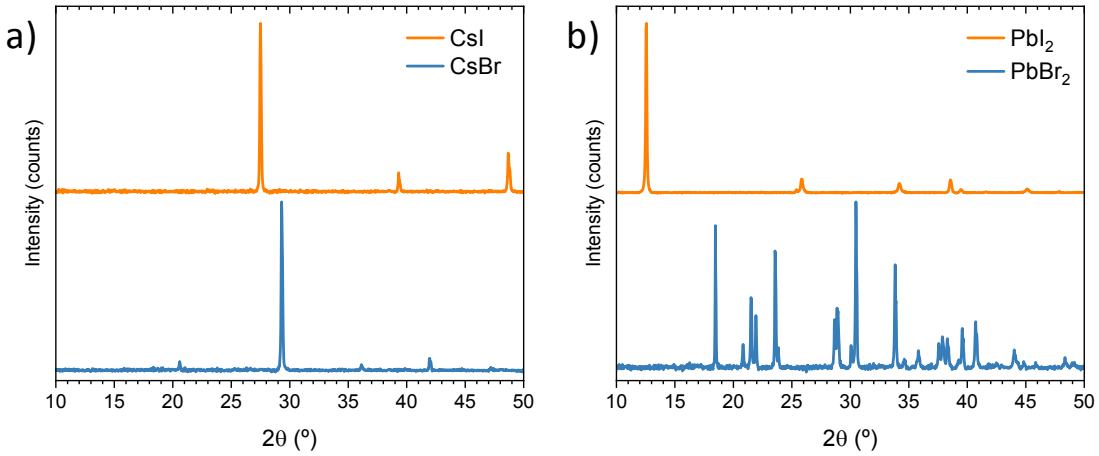

Figure S4. XRD patterns obtained for powders of the pure halide precursors used in this work: a) CsI, CsBr, and b) PbI_2, $PbBr_2$.

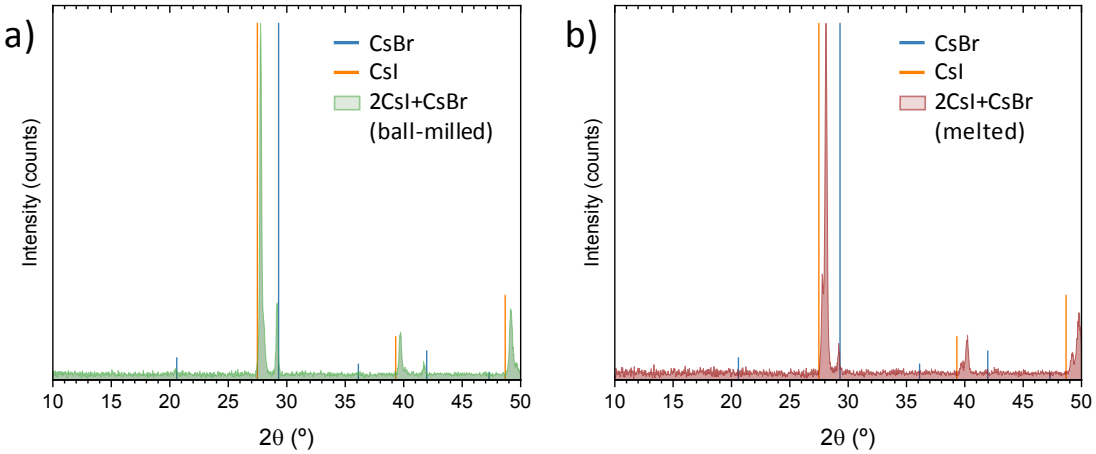

Figure S5. XRD patterns of the products obtained by solid state reactions of 2CsI + CsBr, either by a) ball-milling or by b) melting. The reference diffraction patterns for CsI and CsBr are extracted from the XRD presented in Figure S4a.

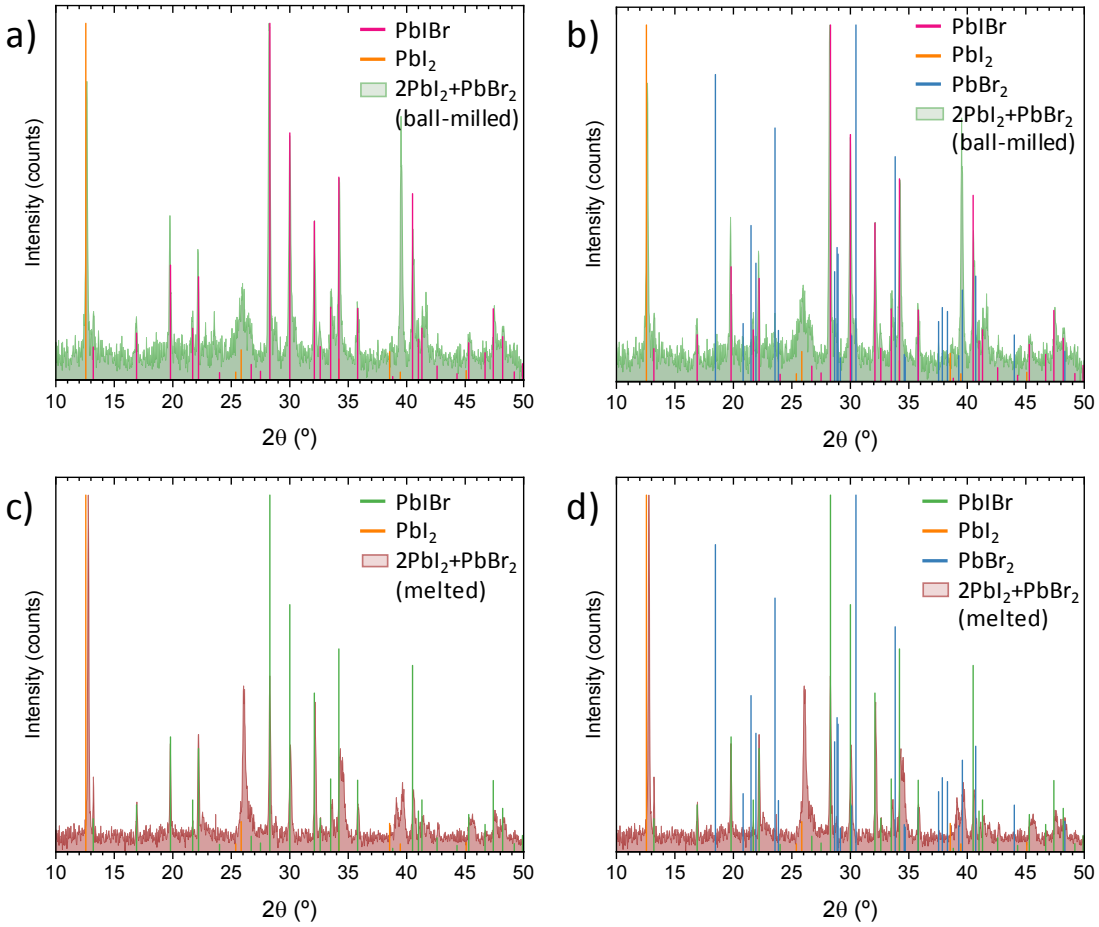

Figure S6. XRD patterns of the products obtained by solid state reactions of $2PbI_2 + PbBr_2$, either by a,b) ball-milling or by c,d) melting. The reference diffraction patterns for PbI_2 and $PbBr_2$ are extracted from the XRD presented in Figure S4b. The reference for the mixed halide PbIBr is taken from the Inorganic Crystal Structure Database (ICSD, Collection Code 22138). In a,c) our reference pattern for $PbBr_2$ was omitted to enhance clarity.

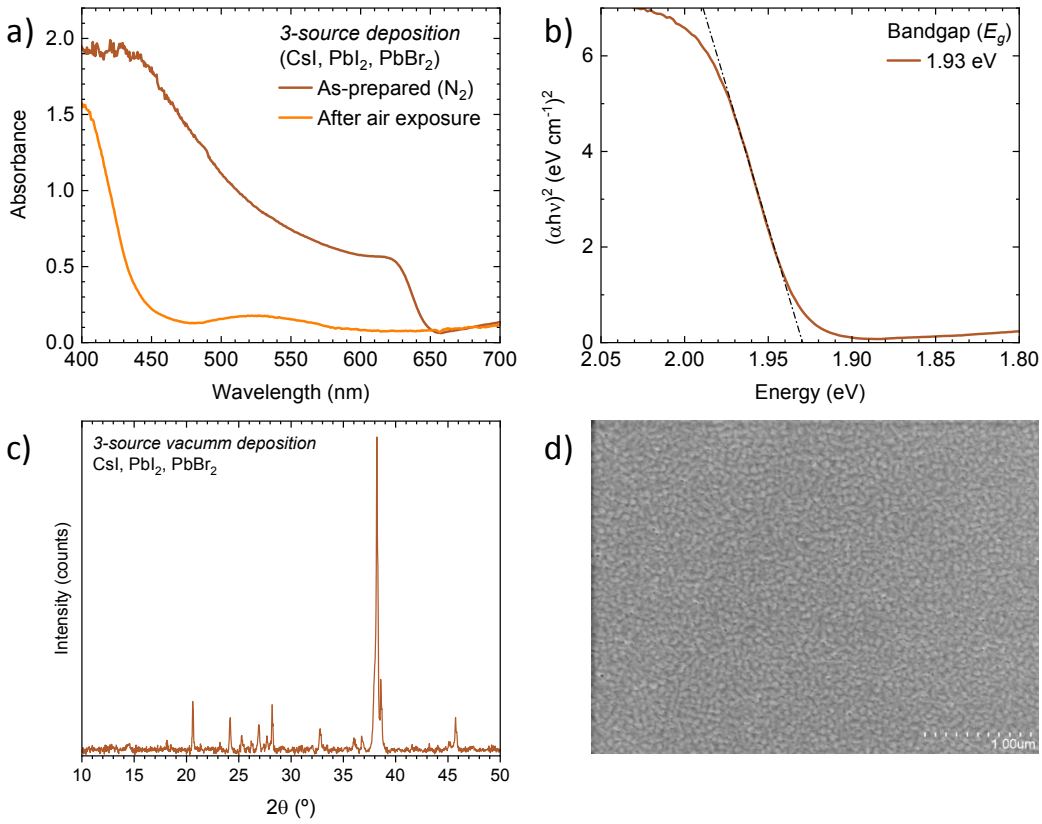

Figure S7. Characterization of $CsPbI_2Br$ films obtained by simultaneous sublimation of CsI, PbI_2 and $PbBr_2$. a) Optical absorption spectra of as-deposited films (brown) and immediately after air exposure (orange). b) Tauc plot for as-deposited films recorded in nitrogen atmosphere, and c) XRD pattern of the film, showing complete degradation of the material upon air-exposure. d) SEM image of an as-deposited film obtained with the same process.

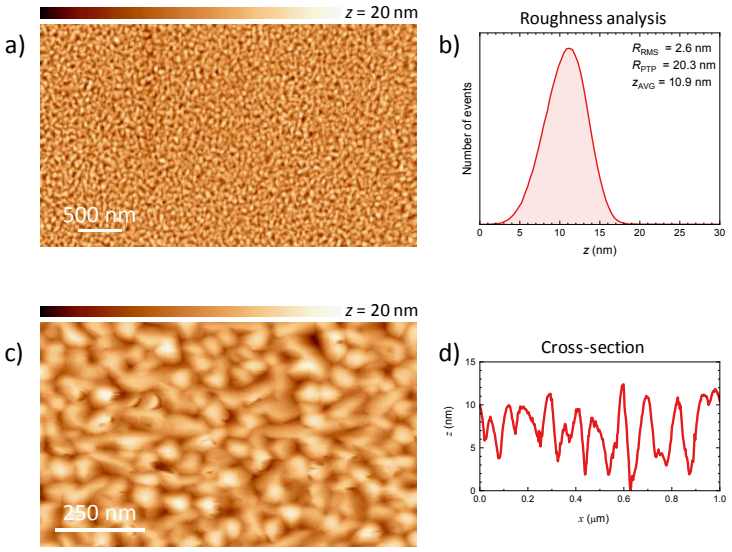

Figure S8. Atomic force microscopy of $CsPbI_2Br$ films prepared by 3-sources fast vacuum deposition at RT. a) Large area topography showing a homogeneous and pinhole-free surface with b) corresponding roughness analysis. c) Higher resolution scan of the sample surface, with d) cross-section trace showing a maximum z variation of approximately 10 nm within the grains.

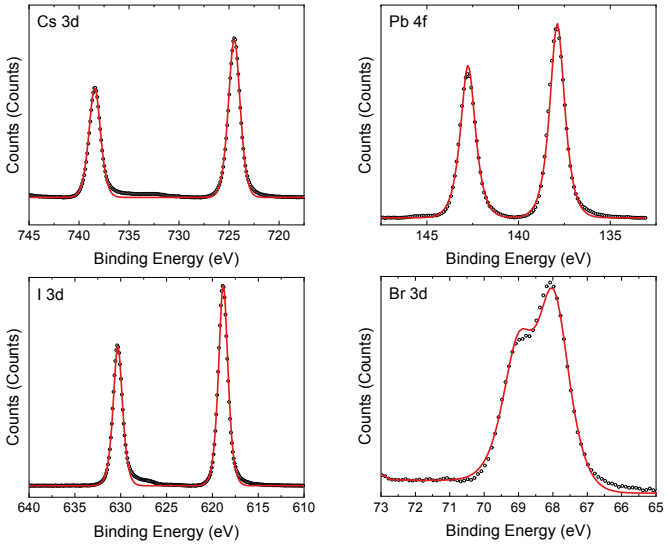

Figure S9. High-resolution XPS spectra of all the main elements as detected from a $CsPbI_2Br$ film obtained by 3-sources vacuum deposition: Cs 3d, Pb 4f, I 3d, and Br 3d regions. The calculated I/Br ratio is 1.8, close to the expected value of 2 for this particular perovskite stoichiometry. We also found an excess of Cs on the perovskite surface (Cs/Pb = 1.7 instead of 1), which is most likely a surface accumulation, as there is no indication of the presence of phase-segregated cesium halides from bulk XRD measurements.

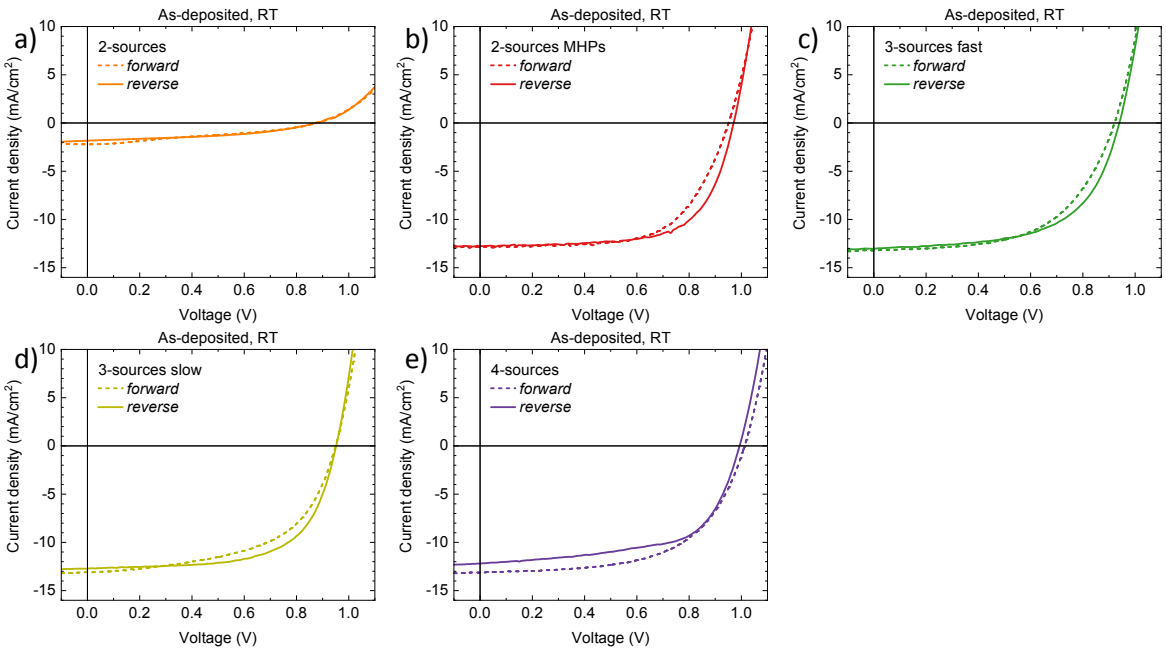

Figure S10. J-V curves in forward (from short to open circuit) and reverse (from open to short circuit) bias for a series of solar cells employing CsPbI2Br deposited at room temperature with the different vacuum techniques.

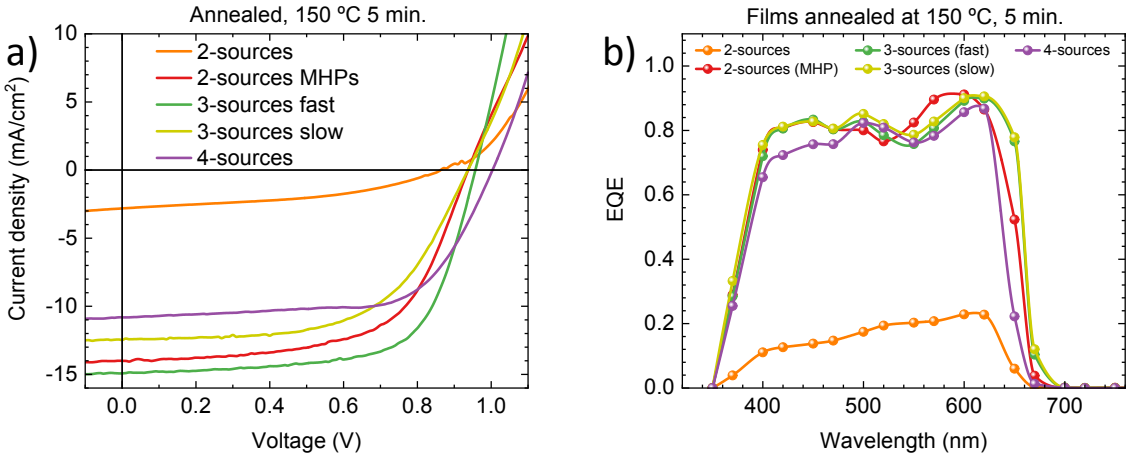

Figure S11. a) J-V curves under illumination in reverse scan and b) corresponding spectral response for the entire series of solar cells with annealed $CsPbI_2Br$ thin films.

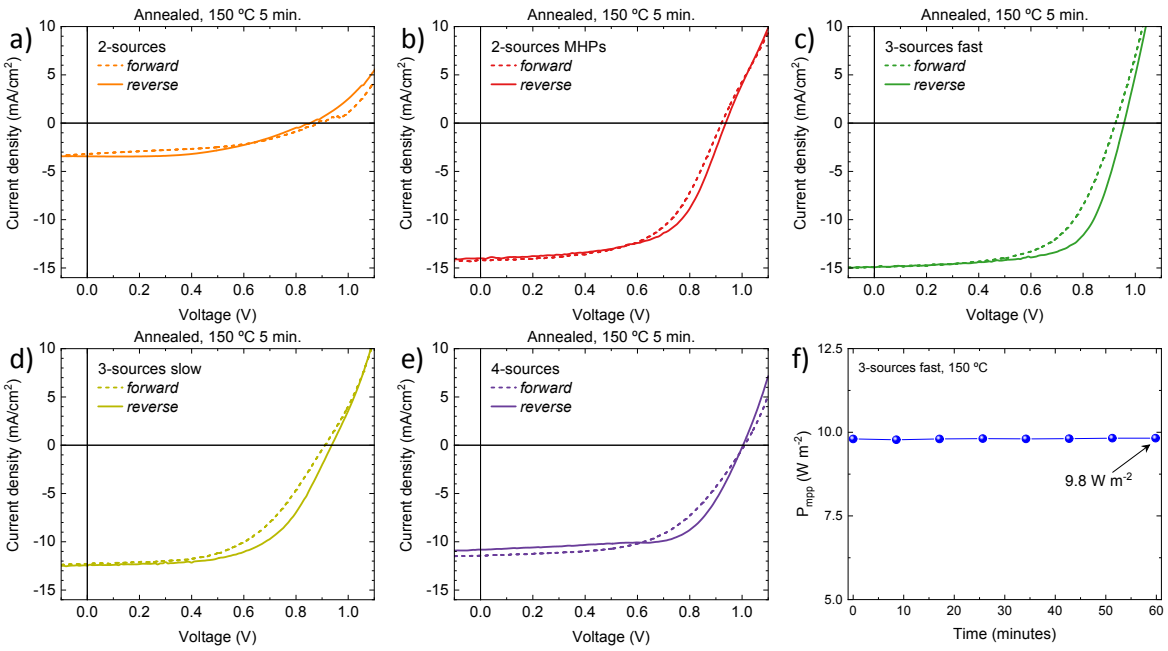

Figure S12. (a-e) J-V curves in forward (from short to open circuit) and reverse (from open to short circuit) bias for a series of solar cells employing CsPbI2Br with annealing at 150 °C for 5 minutes and prepared with the different vacuum techniques. (f) Steady power output under maximum power point tracking for a solar cells with CsPbI2Br prepared by 3-sources vacuum deposition at the rate of 2.0 Å/s (fast) with annealing at 150 °C for 5 minutes (blue).

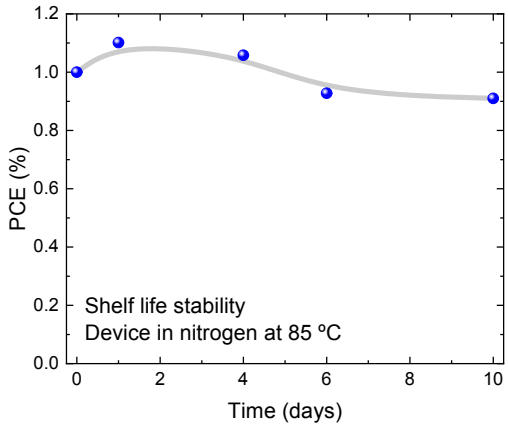

Figure S13. Shelf-life thermal stability measurement obtained by collecting J-V curves at different times for an encapsulated device, stored in nitrogen and in the dark on a hot plate at 85 ºC. The device is based on a $CsPbI_2Br$ film obtained by 3-sources fast deposition and annealed at 150 ºC.

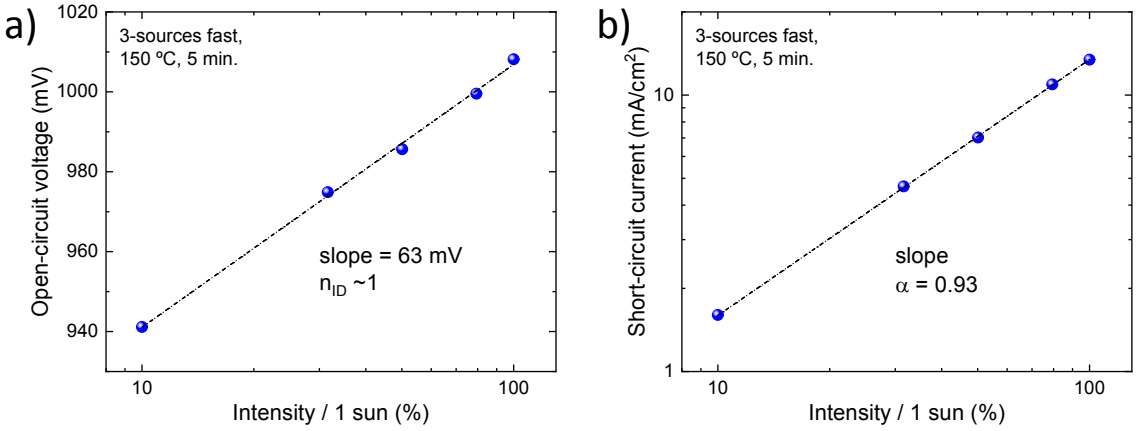

Figure S14. Intensity dependent (a) open-circuit voltage and (b) short-circuit current for a solar cell with a $CsPbI_2Br$ film deposited by 3-sources vacuum deposition at 2.0 Å/s, annealed at 150 °C for 5 minutes. The ideality factor (n_{ID}) is estimated with the slope of the semi-log plot (a), while the short-circuit current in (b) has been fitted with a power law $J \propto I^{\alpha}$, where I is the incident light intensity.

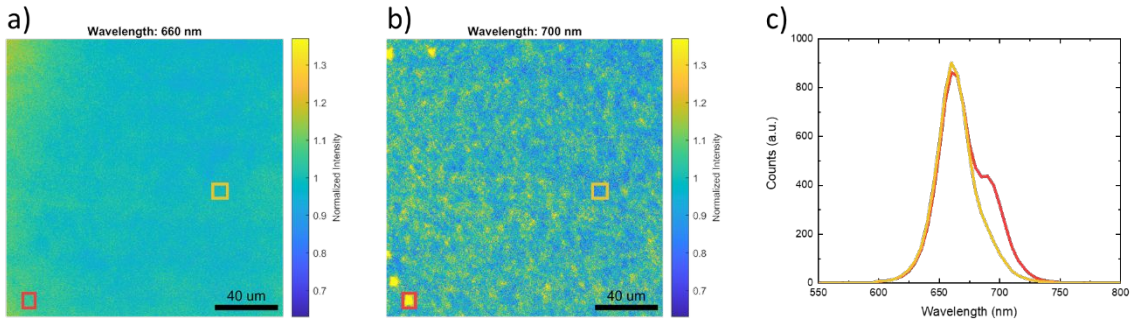

Figure S15. PL maps of a p-i-n solar cells based on $CsPbI_2Br$ (3 sources "fast" with annealing) a) at the wavelength of the main emission (660 nm) and b) at a wavelength of the low energy component (700 nm), which highlight the homogeneity of the $CsPbI_2Br$ film and the inhomogeneous spatial distribution of the low energy emission. Both maps are normalized to their individual mean value. c) Not-normalized spectra at two positions of the map (indicated by the colored boxes) showing the intensity of the low energy feature in few locations and the absence in others.

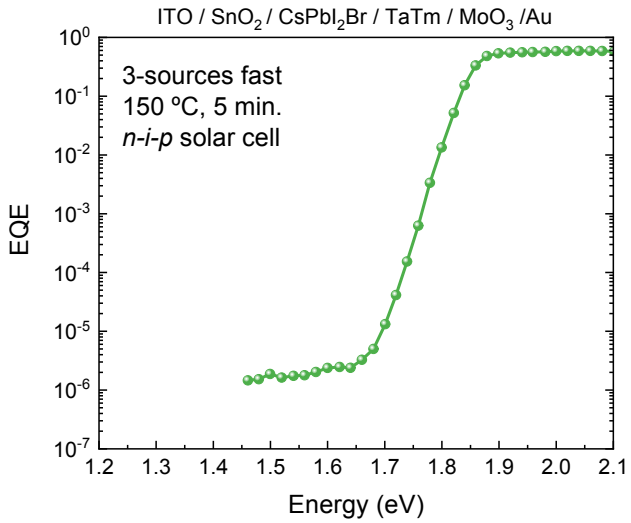

Figure S16. Sensitive EQE spectrum of a n-i-p device with 3 sources "fast" annealed with SnO_2 as ETL and TaTm as HTL, not showing the feature at 1.7 eV as in Fig 4.